Investigation of Transient Gas Dynamics from Laser-Energized Nanoparticles

by

Farzan Memarian

A thesis
presented to the University of Waterloo
in fulfillment of the
thesis requirement for the degree of
Master of Applied Science
in
Mechanical Engineering

Waterloo, Ontario, Canada, 2013

I hereby declare that I am the sole author of this thesis. This is a true copy of the thesis, including any required final revisions, as accepted by my examiners.

I understand that my thesis may be made electronically available to the public.

Abstract

Soot is formed whenever the combustion of hydrocarbon fuels is incomplete. Since soot particles are very small, they can be inhaled and cause severe health problems, such as pulmonary diseases. They can also cause environmental pollution, and have a significant effect on global warming and melting of polar ice sheets. The environmental and health impact of soot depends strongly on soot particle size and morphology, so there is a pressing need for measuring techniques that characterize aerosolized soot.

Laser-Induced incandescence (LII) has proved to be a reliable technique for making spatial and temporal measurements of soot primary particle sizes and soot volume fractions. Nevertheless, there are some unresolved issues in LII, which may cause large errors in soot primary particle size inferred from LII data. One of these issues is anomalous cooling, which is the unexpectedly high initial rate of soot particle cooling observed in experiments, which can not be predicted by LII models. Among the speculations about the possible causes of this phenomenon is the transient gas dynamics effects which have been ignored in LII models. Another phenomena that has been speculated to affect LII predictions in high fluence LII, is how the gas dynamics of sublimed carbon clusters impact the local gas dynamics surrounding the particle during the cooling phase.

The focus of this thesis is to investigate transient effects on heat conduction in low fluence LII, and the gas dynamics of sublimed species in high fluence LII using Direct Simulation Monte Carlo (DSMC) method. DSMC is a statistical/numerical method which works based on the physics of Boltzmann equation. In this method a large number of real molecules are represented by the so called simulated molecules and the state of these

molecules is tracked during the simulation as they undergo collisions with each other and with the boundaries.

The results show that transient effects contribute to anomalous cooling but are not the only cause of this phenomenon. The time scale over which transient effects are significant is also found to be very close to that of anomalous cooling which implies the real cause of anomalous cooling has some similarities to transient effects. Also regarding gas dynamics of sublimation, two effects in particular have been investigated using DSMC, namely, back flux of sublimed species and formation of shock waves. DSMC results confirm the back flux of sublimed species but no shock wave was observed for the boundary conditions considered in this study.

Acknowledgements

I would first like to thank my dear parents. They always gave me the freedom to make my own choices in life and that is why I could follow my own interests. They were so kind that they would do whatever they could for the success of their children as long as it did not interfere with the rights of any other person. They taught me to defend what is right no matter whether it is to my personal advantage or not. They taught me that true success in life cannot be achieved without respecting other people and their rights. Dear mother and father, I am very proud of you not just because you are my parents, but because I believe you have set an example of human beings who are above selfishness.

I would also like to thank my dear sister. She would never hesitate to help me whenever I was in need. Her kindheartedness and humanity was and is always admirable for me. I am deeply grateful for having such a great family with such strong humanitarian ethics which goes beyond any race, religion, country or whatever other means of categorizing human beings.

I also like to express my gratefulness to my supervisor, Dr. Kyle Daun who is indeed an enthusiastic scientist and researcher. His strong work ethics and passion for research was really inspiring for me. I learned from him that if you truly love what you do, you will be successful no matter how hard it may seem. I also learned from him that hard work and being organized will always pay off if also accompanied by strategic planning. I should also thank Professor S. Peterson and J. Wen for reviewing my thesis and providing valuable comments.

I must also thank Dave, Kevin and Fengshan at NRC who kindly provided academic

and finantial support for this research. Their help is greatly appreciated.

I should also express thanks to my dear friend Asad Molayari, who has always been a source of confidence and motivation for me. My good friend, Keyvan Golestan, should also be thanked because he has been a great friend for me during the last two years that we came to know each other, he along with many other good friends made my Masters in waterloo memorable. I also like to thank my officemates, Matt and Tim who were always very nice to me; the atmosphere in our research group was that of helping each other and cooperation.

Table of Contents

List of Figures

Nomenclature

General Symbols

α	Accommodation coefficient
α_d	Thermal diffusivity coefficient
α_{ex}	Exponent in VSS model
a	Soot primary particle diameter
A_s	Particle surface area
β	Effective sublimation coefficient
β	Reciprocal of the most probable molecular thermal speed
$\bar{c}$	Mean thermal speed of the gas
C	Calibration constant
c_0	Speed of light
c_g	Mean thermal speed of the gas
C_r	Radial velocity of molecules interacting with the surface
c_r	Relative velocity between c and c_1
C_s	Specific heat of soot
ΔH_v	Average enthalpy of formation of sublimed carbon species
ΔH_{sub}	Enthalpy of formation of sublimed carbon clusters

δ	Thickness of boundary layer
δ_D	Dirac delta function
d_p	Particle diameter
$\epsilon(c,T)$	Total energy of each molecule
ϵ_a	Fractal exponent
ϵ_λ	Emissivity at wavelength λ
η_{sh}	Shielding coefficient
$E(m)$	A function of the complex refractive index
E_i	Energy flux of incident molecules
E_r	Energy flux of the reflected molecules
E_s	Eenergy flux of diffusive reflection
F	Laser fluence
f	Velocity distribution function
f_a	Fractal prefactor
f_eq	Maxwellian equilibrium velocity distribution
F_{ex}	External force per unit mass
$f_{v,i}(c)$	Velocity distribution functions for incident molecules
$f_{v,r}(c)$	Velocity distribution functions for reflected molecules
f_{v0}	Maxwell-Boltzmann distribution function
Fo	Fourier number
h	Planck constant
$I_{b,\lambda}$	Blackbody intensity
J_λ	Combined incandescence of all particle sizes

$\bar{k}$	Average thermal conductivity
ξ_{int}	Number of active internal degrees of freedom
K_B	Boltzmann constant
k_{ref}	Reference conductivity coefficient
λ	Wavelength
λ_{MFP}	Mean free path
L_c	Characteristic length
μ	Coefficient of viscosity
μ_{ref}	Reference coefficient of viscosity
M	Mass of soot particle
M_v	Mean molecular weight of sublimed species
$\bar{N}_i$	Non-dimensional flux
ν	Collision frequency of gas molecules
n	Number density of gas
N''	Number flux of molecules on the surface
n_g	Equilibrium gas number density
Nu	Nusselt number
$P(a)$	Particle size distribution
p^*	Reference pressure
P_g	Pressure of gas
p_v	Partial pressure of vapor
$\dot{q}_{abs}$	Rate of absorption heat transfer
$\dot{q}_{c,\mathrm{FMR}}$	Rate of conduction heat transfer in free molecular regime

$\dot{q}_{cond}$	Conduction heat transfer rate
$\dot{q}_c$	Continuum heat transfer rate
$\dot{q}_f$	Free molecular heat transfer rate
$\dot{q}_{rad}$	Radiation heat transfer rate
$\dot{q}_{sub}$	Sublimation heat transfer rate
$\dot{q}_{tr}$	Transition heat transfer rate
$q(t)$	Temporal profile of the laser
$Q_{abs,\lambda}$	Absorption efficiency
ρ_s	Density of soot
$R(f)$	Random number
$R(v_i, v_r)$	Scattering kernel function
R_u	Universal gas constant
s	Molecular speed ratio
τ_{eq}	Characteristic equilibrium time of the gas
$\tau_{p,h}$	Characteristic cooling time of the monomer
θ	Angle between the direction of the flux and the surface normal
θ^*	Non-dimensionalized temperature
T^*	Reference temperature
$T_p(t)$	Temperature of the particles
U	Average velocity of the sublimed clusters
v_i	Velocity of the incident molecule
v_r	Velocity of the reflected molecule
ω	VSS scattering index

Acronyms

BGK	Bhatangar, Gross and Krook
DSMC	Direct simulaiton monte carlo
PAH	Polycyclic aromatic hydrocarbons
TEM	Transmission electron microscopy
TiRe-LII	Time resolved laser induced incandescence
VSS	Variable soft sphere collision model

Chapter 1

Introduction

In applications such as power generation, transportation, and waste incineration, where large scale combustion takes place, airborne particles like soot and polycyclic aromatic hydrocarbons (PAHs) are produced. These particles can have significant adverse human health and environmental effects [26, 45]. Also, carbonaceous material, such as black carbon, are sometimes synthesized deliberately by using fuel-rich combustion for some applications [2].

1.1 Objectives of Studying Soot

There are two major objectives for studying soot, the first one is to increase the efficiency of combustion processes, i.e., reducing pollution and optimizing conversion of energy. The second one is for synthesizing carbonaceous material of specific properties which requires controlled operating conditions. Fundamental to any research about soot is a qualitative

and quantitative understanding about the chemical processes involved in oxidation and formation of hydrocarbons, and in depletion of PAH and soot [2, 47]. A concise review of the formation of soot will be offered in the next section.

1.2 Soot Formation

PAHs are generally considered to be an intermediate step in formation of soot [47, 46, 17]. Currently, it is accepted that there are three partially-parallel processes in soot formation:

- The first one is "particle nucleation". In this stage, larger PAHs are produced by chemical reactions of smaller PAH's radicals with each other, or with acetylene. When PAHs reach a certain size, they react with each other, but in parallel the grows of individual PAHs continues, it's this stage where particle nucleation occurs.

- The second stage of soot formation is "surface growth". It is the reactions that happen at the surface of the growing particles that cause significant build-up of mass which is mainly carbon. These reactions are believed to have the same nature as reaction between PAHs [17]. PAH and acetylene are considered to be species that contribute to particle growth [4, 23]. As the size of the particle increases the rate of surface growth begins to decline.

- Then there is the final stage of soot formation and growth, i.e. "aggregation". When spherical soot primary particles reach a certain size and their growth is stopped, some of them stick together as a result of collision and form large fractal structures [17]. Fig 1.1 is a picture of a typical soot aggregate which is composed of a number of primary

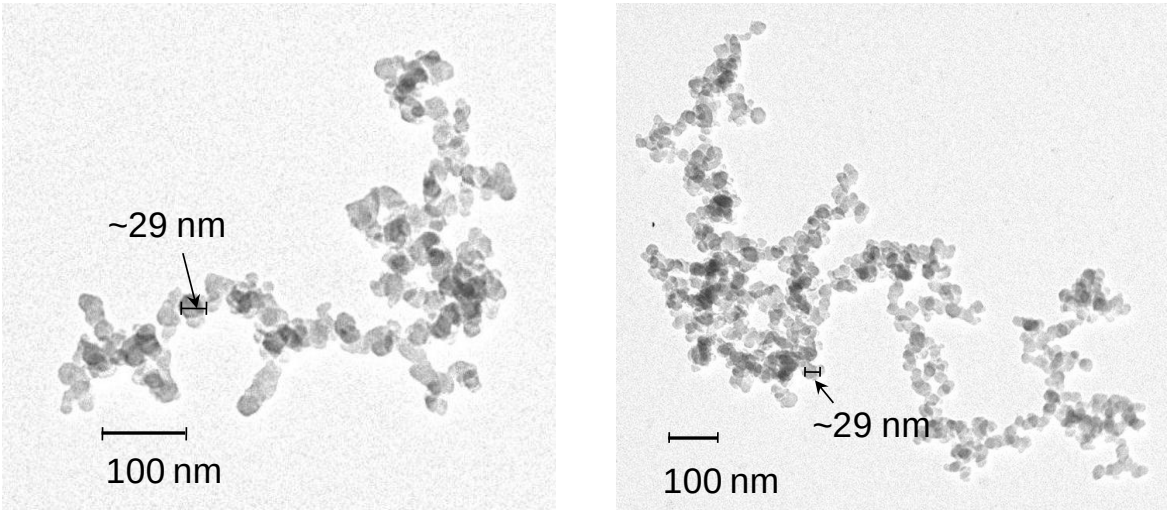

Figure 1.1: Typical soot aggregates, courtesy of Dashan Wang, National Research Council, Canada [10]

particles. The morphology and size of soot is strongly affected by the conditions governing its formation stage in the combustion process and hence it will be differ depending on the fuel, engine and any other parameter affecting the combustion process.

1.3 Soot in Combustion

As mentioned before, soot is produced when the combustion of fuel is incomplete which is undesirable if the only goal of combustion is to produce useful work. The presence of soot implies a low energy production efficiency of combustion.

Nonetheless, depending on the combustion application, soot can have a desirable or un-

desirable heat transfer effect. In a boiler where increased rate of heat transfer is favorable, the presence of soot can be useful in the combustion flame, since it increases the rate of radiation heat transfer to the walls of the combustion chamber and hence facilitates heat transfer to the working fluid. The example of one application where presence of soot is unfavorable is internal combustion engine since any increase in the rate of heat transfer will decrease the efficiency of the engine [52].

1.4 Health Effects

Soot particles are so tiny that they can easily be inhaled and, consequently, be deposited in the lungs; the PAHs that are desorbed on the surface of soot are carcinogenic and hence dangerous for human health [3]. It is also shown by epidemiological studies that being exposed to high levels of aerosol matter can lead to various pulmonary diseases, such as bronchitis, asthma and viral infections [56].

Due to the health hazards of aerosol particles, many countries have regulated particulate emission and hence the mass concentration of soot has decreased in the atmosphere in North America. The worrisome fact, however, is that it is not only the mass concentration of soot that is dangerous but the size of individual primary particles and aggregates is also important. Most of the techniques used for reducing the mass concentration of soot work based on decreasing the size of individual soot particles and the smaller the soot particles the more their ability to penetrate the respiratory system tissue. A study by Sue et al, shows that the toxicity level of soot increases by decreasing the size of soot particles [58].

1.5 Environmental Effects

Recent studies have examined the effect of combustion-generated soot on climate, and in particular on global warming. Deposited soot on the surface of polar ice decreases the reflectivity coefficient of ice and hence it will absorb more radiation energy from sun and reflect less which will cause an increase in its temperature and consequently melt the ice. It is also proposed that the embedded soot in snow or ice can decrease its reflectivity and lead to its melting [20].

1.6 Measuring and Detection Techniques

The function of soot in combustion and its effect on environment and health is related to soot morphology. Hence one important aspect of research on soot is quantifying its size distribution and concentration. The measuring technique used for quantifying soot particulates must have certain characteristics to make it reliable and applicable, for example, it must be able to measure the particulate emission in a wide range of size distributions and concentrations, and it must work well in different physical conditions, such as in situ combustion exhaust, and ambient air.

There are several methods for measuring the particle concentration or size distribution such as filtered Rayleigh scattering, transmission electron microscopy (TEM), laser attenuation and laser induced incandescence (LII). The focus of the current study is on LII and there will be a through description of this method in the following paragraphs.

1.7 Laser-Induced Incandescence

Time-resolved laser induced incandescence (TiRe-LII) is a diagnostic mainly used for measuring the concentration and size distribution of soot primary particles for a wide range of combustion applications that include in-cylinder combustion, laminar and turbulent diffusion flames and engine exhaust gas characterization [57, 50].

In this method, a laser pulse lasting several nanoseconds heats a sample volume of aerosol, and the resulting spectral incandescence is measured using collection optics and photo detectors as the nanoparticles cool via heat transfer to the surrounding gas. Since smaller nanoparticles cool more rapidly than larger ones, it is possible to infer the effective particle size distribution from the observed incandescence decay rate, provided the heat transfer rate from the particles to the surrounding gas is known.

Soot volume fraction can be measured easily using this technique since it is shown to be approximately proportional to the incandescence signal in the visible wavelength bandwidth [36]. To make this proportionality an equality and get a quantitative measurement of the soot volume fraction, the signal needs to be calibrated.

The situation is much more complicated for measuring the size of the primary soot particles. In this case the technique used is often called time-resolved laser-induced incandescence (TiRe-LII). After the laser pulse, the laser energized nanoparticles cool by heat transfer to the surrounding gas by different mechanisms such as conduction and sublimation in case of high fluence LII. Due to the difference in their capacity for storing thermal energy, smaller particles tend to cool down faster than larger particles and this difference is used to infer the size of the particles based on the decay of the incandescence signal

[8, 36, 64, 48]. Inferring the size of particles by interpreting the decay of the signal is much more difficult than inferring the soot volume fraction. Analogous to the method used for soot volume fraction measurements, some researchers have tried to calibrate primary particle sizes by comparing the results with that of transmission electron microscopy (TEM) for flames that the latter can also be used [62]. This method is very lengthy and difficult in practice, so most of the time a theoretical model of TiRe-LII is used for primary particle size evaluation.

The time resolved signal for the laser-heated particles is theoretically predicted by a model which includes heat and mass transfer mechanisms. Melton presented a model in 1984 [36] which models the temperature and signal variations for a single spherical particle that is heated by a laser pulse of nano-seconds duration. Heat and mass balance equations are considered in this model.

Smallwood et al. [54] did some improvements to modeling sublimation in 2001. Sublimation happens if the temperature of the particle increases above the sublimation temperature and usually it is only significant when laser fluence is high. Sublimation is assumed in their model to be only a function of the surface temperature and hence it is considered as a surface phenomenon.

There are some challenges in modeling the conduction heat transfer from the hot particles to the background gas and different treatments have been suggested in this regard. In general there are three heat transfer regimes, namely, free molecular, continuum and transition regime; these regimes and their difference will be explained in more detail in the next chapter. In most LII applications, the heat transfer regime is neither continuum nor free molecular for both of which theoretical models of heat transfer are well developed, it

happens in the transition regime and there is no universally-accepted formula for calculating heat transfer rate at this regime [15]. There are some other mechanisms involved in LII which can potentially affect the measurements; Michelsen in her 2003 paper [41] has done a comprehensive review of all the mechanisms that are involved in particle heating and subsequent cooling. Not only sublimation has been treated meticulously, the possible effect of some other mechanisms such as oxidation and thermal annealing has been investigated. Now that some background has been provided for the general logic of LII method, there will be a more detailed description of the way size distribution of particle can be estimated by TiRe-LII.

Time-resolved laser induced incandescence infers the particle size distribution in the aerosol, $P(a)$, from the measured incandescence of laser-energized particles as they re-equilibrate with the surrounding gas. At any instant in the cooling process the LII signal is due to the combined incandescence of all particle sizes,

$$J_\lambda(t) = C \int_0^\infty \pi a^2 P(a) Q_{abs,\lambda}(a) I_{b,\lambda}[T_p(t,a)] da \tag{1.1}$$

in which $Q_{abs,\lambda}$ is the absorption efficiency and C is a calibration constant that depends on the particle loading, excitation laser fluence, and detector optics, $T_p(t)$ is the temperature of the particles at time t, $I_{b,\lambda}$ is the corresponding blackbody intensity

$$I_{b,\lambda}(T_p) = \frac{2hc_o^2}{\lambda^5}\left[\exp\left(\frac{hc_o}{\lambda k_B T_p}\right) - 1\right]^{-1} \tag{1.2}$$

and $P(a)$ is the distribution of aerosol particle radii. The size distribution can be found

by nonlinear regression of modeled spectral incandescence to experimental measurements [13]. The modeled incandescence is found using calculated cooling curves for a range of particle sizes. These curves can be found by integrating the ordinary differential equation

$$\rho_s C_s \frac{\pi}{6} d_p^3 \frac{\mathrm{d}T}{\mathrm{d}t} = \dot{q}_{abs}\left(t,a\right) - \dot{q}_{cond}\left(t,a\right) - \dot{q}_{rad}\left(t,a\right) - \dot{q}_{sub}\left(t,a\right). \tag{1.3}$$

the left hand side of Eq. (1.3) is the change in internal energy of a single primary particle in which ρ_s is the density and C_s is the specific heat of soot, T is the instantaneous soot temperature and d_p is the diameter of the primary particle. The right hand side terms refer to absorption, conduction, radiation and evaporation/sublimation heat transfer rate respectively. The laser energy absorption rate [40] for a single primary particle is given by

$$\dot{q}_{abs} = \frac{\pi^2 d_p^3 E(m)}{\lambda_1} \frac{F q(t)}{q_1}, \tag{1.4}$$

where $E(m)$ is a function of the complex refractive index, $q(t)$ is the temporal profile of the laser which has been normalized to 1, F is the laser fluence and λ_1 is the laser wavelength. The second term on the right hand side of Eq. (1.3) is rate of conduction cooling and depending on whether the heat transfer is happening in continuum, free molecular or transition regime is treated accordingly. More details about modeling conduction heat transfer will be presented in the following chapters. Then there is radiation heat transfer, $\dot{q}_{rad}$. The approach used in all LII models is to integrate the Plank function over all wavelengths in order to calculate the rate of emission of radiative energy from the particle

[40],

$$\dot{q}_{rad} = \pi D^2 \int_0^\infty \epsilon_\lambda \frac{2\pi hc^2}{\lambda'^5 \left[exp\left(\frac{hc}{\lambda' k_B T}\right) - 1\right]} \, \mathrm{d}\lambda' \tag{1.5}$$

where ϵ_λ is the the emissivity at a wavelength λ, h is the Planck constant (6.626×10^{34} m^2 kg/s), c is the speed of light in vacuum, and k_B is the Boltzmann constant. Many LII models use the Rayleigh approximation to substitute for emissivity and equation (1.5) will simplify by further assuming that E(m) is wavelength independent to

$$\dot{q}_{rad} = \frac{199\pi^3 D^3 \left(k_B T\right)^5 E(m)}{h(hc)^3} \tag{1.6}$$

Radiation heat transfer from heated soot particles is neglected in most LII applications and is also neglected in the current study. The fourth term on the right hand side of the energy balance equation (1.3) is the rate of sublimation heat transfer which can be found from

$$\dot{q}_{sub} = -\frac{\Delta H_\nu}{M_\nu} \frac{\mathrm{d}M}{\mathrm{d}t}, \tag{1.7}$$

where the rate of mass loss can be found from

$$\frac{\mathrm{d}M}{\mathrm{d}t} = \frac{1}{2}\pi d_p^2 \rho \frac{\mathrm{d}d_p}{\mathrm{d}t} = -\pi d_p^2 \rho \beta_{sub} p_\nu \sqrt{\frac{M_\nu}{2\pi R_u T}} \tag{1.8}$$

in which M is the mass of the soot particle and ΔH_v is the average enthalpy of formation of sublimed carbon species. M_v is the mean molecular weight of sublimed carbon clusters [57]. β_{sub} is the effective sublimation coefficient which is taken to be 0.9 in [54], R_u is the universal gas constant.

There are some uncertainties in low fluence and high fluence LII, such as the unknown

effect of transient conduction in low fluence LII and the gas dynamics effects of sublimed species in high fluence LII. In order to address these uncertainties which will be described in more detain in the next chapter, transient Direct Simulation Monte Carlo (DSMC) simulations have been used as a strong numerical tool.

1.8 Introduction to DSMC

DSMC is a stochastic/numerical method which is based on the physics of high Knudsen number flows and the assumptions made in derivation of Boltzmann equation which governs gas molecular dynamics surrounding the laser-energized nanoparticles; it does not give an explicit solution of Boltzmann equation, but the result that it yields is the same as solving the Boltzmann equation [7].

In this method, like most other computational methods, the computational domain is spatially divided by a number of computational cells. These computational cells are intended for two purposes. First, the probable collision pairs are chosen within each cell and second, the statistical information that is gathered accumulatively from the velocity distribution of molecules within each cell, is averaged and processed to give the macroscopic properties at the center of that cell. A time step needs to be chosen which can vary during the simulation or be constant. One of the basics assumptions in DSMC is that over a sufficiently small time step, molecular motion and collisions can be assumed to be independent of each other. For this assumption to be valid, the time step must be only a fraction of the mean collision time, and also be sufficiently small so as not to allow the molecules to move a distance larger than the cell dimensions in a single time step.

The boundary conditions should be able to model the real physics of the problem which can be an imposed temperature on a wall or boundary, a pressure on a boundary, a moving surface or even a vacuum boundary. When the initial condition is chosen and the boundary condition is defined, the simulation will march and model the evolution of the flow field from the initial conditions based on the imposed boundary conditions. There is an initial period where the transient effects happen and that period is neglected in steady DSMC simulations and is not considered in the final sampling of parameters, it is only the samples after that period which go through a time and ensemble averaging to give the macroscopic quantities such as temperature, pressure, density, heat transfer and etc. Since DSMC simulation is a stochastic method, it needs a sufficiently large sample size to be able to calculate the macroscopic properties in each cell, this is why the simulation continues for a large number of sampling periods after the steady state is reached to yield a large sample size for each cell. Now it is useful to see how DSMC actually models the evolution of flow field.

By passage of each time step, the ballistic molecular motions are calculated deterministically based on the last velocity stored for each molecule, and then intermolecular collisions between molecules and interactions with boundaries are considered. Contrary to molecular motion, intermolecular collisions are calculated stochastically, i.e. each pair that is chosen has a probability of collision that is proportionate with its relative velocity; DSMC only allows binary collisions which is a good model of the physics of diluted gases. The position, translational velocity and internal energy of each molecule is stored and tracked as the simulation continues. Each time an intermolecular collision or boundary interaction happens, the velocity and internal energy of the engaged molecules are updated. Since

the number of real molecules is normally very large and modeling the transport process of all of them individually is computationally expensive, the concept of simulated molecules is used; each simulated molecule models the transport process of a large number of real molecules.

1.9 Objective and Scope of Thesis

The purpose of this thesis is to use transient DSMC simulations to investigate some of the unresolved issues in LII, namely transient heat conduction effects, back flux of sublimed species and the formation of shock waves. Chapter 2 provides background concerning transition regime heat transfer and sublimation in low and high fluence LII. In this chapter, Boltzmann equation is introduced first, and then heat transfer regimes (free molecular, continuum and transient) and their underlying physics are discussed. Then different methods for modeling heat transfer in the transition regime which include, approximate analytical techniques, interpolation techniques, two-layer technique, and numerical techniques are explained. Then sublimation in LII is presented followed by a discussion about different sources of uncertainty in LII, specially sublimation.

Chapter 3 is focused on the numerical simulation of transient transition regime heat conduction in LII. In this chapter, the importance of transient effects is investigated first using an scale analysis proposed by Filippov and Rosner [15], then the transient DSMC method used in this thesis is explained in detail and the results of the simulation are presented afterwards. At the end of this chapter the scale analysis of Filippov and Rosner [15] is re-evaluated and an alternative more physical analysis is provided.

Chapter 4, discusses sublimation in high fluence LII. First different computational parameters in the DSMC simulation are explained. Then the model used for simulating intermolecular collisions is described. At the end there is a section in which the results are presented and discussed.

Finally chapter 5 is dedicated to conclusion of the previous chapters and proposing the research path that can be taken in future.

Chapter 2

Background Information

2.1 Introduction

In this chapter, the physics of heat transfer in LII is discussed. First the governing Botltzmann equation is introduced and then different heat transfer regimes are discussed. Different methods for modeling heat transfer in the most intractable regime, which is the transition regime, are presented. Then the physics of sublimation is explained and at the end the unanswered phenomena and sources of uncertainties in LII are presented.

2.2 Governing Equations for Heat Transfer in LII

The Boltzmann equation, is the governing equation for all different heat transfer regimes. The complete Boltzman equation [7] for a dilute gas is written as

$$\frac{\partial}{\partial t}(nf) + \mathbf{c}\frac{\partial}{\partial r}(nf) + \mathbf{F_{ex}}\frac{\partial}{\partial c}(nf) = \int_{-\infty}^{+\infty}\int_{0}^{4\pi} n^2\left(f^* f_1^* - f f_1\right) c_r \sigma \mathrm{d}\Omega \mathrm{d}c_1 \tag{2.1}$$

in which n is the number density of gas, f is the velocity distribution function which is a the short form for $f(c, r, t)$, f_1 is also the short form for $f(c_1, r, t)$. c_r is the relative velocity between c and c_1 which is given by $c - c_1$.

The first term in the left hand side of equation (2.1) is the total rate of increase of the number of molecules in the velocity-space element $\mathrm{d}c.\mathrm{d}r$. The second term is the net outward flow of molecules of class c across the boundary of $\mathrm{d}r$ due to velocity c. The third term is the net outward flow of molecules across the surface of $\mathrm{d}c$ due to external force F per unit mass. In case of LII simulations, there is no significant external force so the third term is negligible. The right hand side of equation (2.1) has a single term which is the *collision term*. Since it has an integral form in contrary to the differential form of the left hand side terms, it is the cause of the mathematical difficulty in solving the full Boltzmann equation.

2.3 Review of Heat Transfer Regimes in LII

Heat transfer in LII, can take place in three different regimes. the non-dimensional number that determines heat transfer regime is the Knudsen number, Kn, which is the ratio of two

length-scales

$$Kn = \frac{\lambda_{MFP}}{L_c} \tag{2.2}$$

where λ_{MFP} is the mean free path which is the average distance a molecule travels between two successive collisions with other molecules, and L_c is the characteristic length of the problem. Modeling heat transfer in LII is mainly concerned with simulating heat transfer from a single primary particle or an aggregate, hence the characteristic length is the radius (or diameter) of the particle or aggregate. The diameter of primary soot particles in most LII applications is in the range of 10-60 nm. In general there are three heat transfer regimes which will be discussed briefly.

2.3.1 Free Molecular Regime Heat Transfer

If the Knudsen number is ~ 10 or greater, the mean free path is several times the particle radius and hence the heat transfer between the particle and the surrounding gas occurs in the free molecular regime.

This heat transfer regime happens when the LII experiment is done at flames with pressures of the order of or below atmospheric pressure. As one example of such conditions, if $P_g = 1$ atm and $T_g = 1700$ K, the mean free path of the background gas is about 580 nm which is much larger than the radius of soot particles. As a result of the very large ratio of these two length-scales, the molecules can ballistically travel large distances between the particle and the equilibrium gas without undergoing inter-molecular collisions. Since the size of the particle is much smaller than the mean free path of molecules, the probability that a molecule collides on the surface of the particle is very low. But in case a

collision between a molecule and the surface occurs, that molecule will easily transfer the energy that has absorbed from the particle to the bulk gas without undergoing collisions with other molecules in the vicinity of the surface. Therefore, the rate of free-molecular heat conduction depends on the incident molecular number flux as well as the energy transferred when a gas molecule collides with a surface, which is specified by the thermal accommodation coefficient, α [31]. α is an indicator of the amount of adjustment between the temperature of the incident molecule with that of the surface. If $\alpha = 1$, it means complete energy adjustment and if $\alpha = 0$ there will be no energy adjustment. α can be written as

$$\alpha = \frac{E_i - E_r}{E_i - E_s} \tag{2.3}$$

where E_i is the energy flux of incident molecules, E_r is the energy flux of the reflected molecules and E_s is the energy flux that would exist if the reflection was completely diffuse and the maximum energy transfer allowed by the second law of thermodynamics would happen [12].

In general, the rate of conduction heat transfer from the surface of the heated soot particle can be written as [31]

$$\dot{q}_{c,\mathrm{FMR}} = A_s \left[\int_{C_r<0} \epsilon(c, T_g) C_r f_{v,i}(c) \mathrm{d}c + \int_{C_r>0} \epsilon(c, T_p) C_r f_{v,r}(c) \mathrm{d}c \right] \tag{2.4}$$

in which A_s is the particle surface area, $4\pi a^2$, $\epsilon(c, T)$ is the total energy of each molecule which is the sum of translational, rotational and vibrational energies, C_r is the radial velocity of molecules interacting with the surface and $f_{v,i}(c)$ and $f_{v,r}(c)$ are the velocity

distribution functions for incident and reflected molecules respectively. The velocity distribution for incident molecules in the free molecular regime could be assumed to be an equilibrium Maxwell-Boltzmann distribution but the velocity distribution of the reflected molecules depends on the model used for describing the surface interaction. In general, the velocity distribution of the reflected molecules is described by the following equation [15]

$$f(v_r) = \int_{v_i n<0} R(v_i, v_r) f(v_i) \mathrm{d}v_i \tag{2.5}$$

where v_r is the velocity of the reflected molecule and v_i is the velocity of the incident molecule, n is the normal unit vector to the surface of the particle and $R(v_i, v_r)$ is the scattering kernel function. The scattering kernel is defined so as to account for momentum and energy accommodation of molecules colliding with the surface. Usually Maxwell's model is used for defining the scattering kernel, hence the scattering is modeled as a combination of specular and diffuse reflection as follows

$$R(v_i, v_r) = \alpha f_{eq}(v_r, T_p) \left|vn\right| + (1-\alpha)\delta_D(v_i - v_r + 2n[nv_r]) \tag{2.6}$$

where δ_D is the Dirac delta function and f_eq is the Maxwellian equilibrium velocity distribution [15] which is given by

$$f_{eq}(v_r, T_p) = \left(\frac{m}{2\pi k T_p}\right)^{3/2} exp\left(-\frac{m v_r^2}{2kT_p}\right) \tag{2.7}$$

Now returning back to equation (2.4), the first term on the right hand side is the integration over the energy transfer to or from all the molecules that are incident on the

surface and the second term is for energy transfer to or from the molecules that are reflected form the surface. Equation (2.4) can be written in a more simplified format as

$$\dot{q}_{c,\mathrm{FMR}} = A_s N'' \langle E_i - E_r \rangle \tag{2.8}$$

where N'' is the number flux of molecules on the surface which is given by $n_g c_g/4$ in which $n_g = P_g/(k_B T_g)$ is the equilibrium gas number density, and $c_g = [8k_B T_g/(\pi m_g)]^{1/2}$ is the mean thermal speed of the gas. Using the definition of α in Eq. (2.3), the free molecular heat transfer rate can be expressed as

$$\dot{q}_{c,\mathrm{FMR}} = \pi a^2 n_g c_g k_\mathrm{B} \alpha \langle E_i - E_s \rangle \tag{2.9}$$

Eq. (2.9) can be simplified by substituting for $\langle E_i - E_s \rangle$ to get

$$\dot{q}_{c,\mathrm{FMR}} = \alpha \pi a^2 n_g c_g k_\mathrm{B} \left(2 + \frac{\xi_{int}}{2}\right) (T_p - T_g) \tag{2.10}$$

where ξ_{int} is the number of active internal degrees of freedom involved in the gas/surface scattering. Equation (2.10) can be further simplified by substituting in for number density $n = p_g/k_B T_g$ and mean molecular speed $c = [8k_B Tg/(\pi m_g)]^{1/2}$. The number of active internal degrees of freedom can also be expresses in terms of γ where $\gamma = (\xi_{int}+5)/(\xi_{int}+3)$, so that

$$\dot{q}_{c,\mathrm{FMR}} = \alpha \pi a^2 \sqrt{\frac{2k_B T_g}{\pi m_g}} \left(\frac{\gamma + 1}{\gamma - 1}\right) \left(\frac{T_p}{T_g} - 1\right) \tag{2.11}$$

2.3.2 Continuum Regime Heat Transfer

If conditions are such that the Knudsen number is of the order of 0.01 or smaller, continuum heat transfer will occur between the heated nanoparticle and the surrounding gas. It is very rare in LII applications to meet continuum regime heat transfer because it requires unusually high pressures of the order of 100 atm which do not usually exist in practical applications.

If the heat transfer regime is continuum, molecules that are being incident on the surface experience several inter-molecular collisions before reaching the surface and molecules that are reflected from the surface will also undergo numerous collisions in a short distance from the surface. The molecules will not travel ballistically in this case due to their small mean free path and their motion is similar to a random walk. Heat transport from the particle has two stages, stage one is energy transfer between the colliding particles and the surface and the second one is the transport of that absorbed energy in the gas further away from the surface of the particle.

In case of continuum heat transfer, the number flux of incident molecules is so high that the first step will not limit the rate of heat transfer, unlike the free molecular heat transfer, it is the second stage that limits the rate of heat transfer; energized molecules which are moving away from the surface will face a barrier by other molecules and numerous intermolecular collisions slows down the transport of energy within the gas. The second stage is called diffusion and the speed of diffusion of a gas at any state is limited [31]. One can solve the stationary continuum heat transfer equation (which is independent of the momentum equation) for heat transfer from the spherical particle with its quiescent

surrounding gas and get [15]

$$\dot{q}_{cont} = 4\pi a \bar{k} \left[T_p - T_g\right] \tag{2.12}$$

where $\bar{k}$ is the the average thermal conductivity between T_p and T_g.

2.3.3 Transition Regime Heat Transfer

In many TiRe-LII experiments carried out on high pressure aerosols, such as those in engine combustion chambers, Kn is ~ 1 and heat transfer takes place in the transition regime (which is between free molecular and continuum regime). In this regime, heat conduction has some similarities to both continuum and free molecular regime; it is affected by the rate of incidence of gas molecules on the surface of the particle (similar to free molecular regime) and by the frequency of intermolecular collisions (similar to continuum regime).

For transition regime heat transfer, in contrast to the free-molecular regime, the governing Boltzmann equation does not reduce to an analytically-tractable form, because the full Botlzmann equation which is a nonlinear integral-differential equation needs to be solved using appropriate initial and boundary conditions and there is nodirect analytical way for doing that; LII researchers must instead rely on approximate methods. Models developed for evaluating heat transfer in transition regime fall under one of these categories: interpolation methods, approximate analytical methods, and two layer or boundary sphere methods [31].

Before discussing different methods of estimating the heat transfer rate in the transition regime, it is useful to compare the dependence of heat transfer rate to the Knudsen number for different heat transfer regimes. Figure 2.1 shows steady state heat conduction from a

particle at constant temperature to the surrounding gas over a range of Knudsen numbers, expressed in dimensionless form as the Nusselt number,

$$Nu = \frac{q}{4\pi k\left(T_g\right) a\left(T_p - T_g\right)} \tag{2.13}$$

in which $k(T_g)$ is the temperature dependent conductivity coefficient of the gas. In Figure 2.1, the Nusselt number for the transition regime has been derived from Fuchs's boundary sphere method which will be described later. It can be observed from this figure that continuum regime heat transfer rate is not affected by Knudsen number but in case of free molecular regime, a strong linear dependence on Knudsen number is seen.

The three heat transfer regimes have been discussed and now different techniques for modeling heat transfer in the transition regime will be explained in the following paragraphs.

2.3.3.1 Approximate Analytical Techniques

Bird [7] has discussed some of these methods in his book at 1994. Three general approaches have been developed for this purpose which are:

- model equation method
- small perturbation method
- moment method

These methods are used in conjunction with each other in most of the cases. The purpose of the model equation is to make the collision term less complicated and the most famous

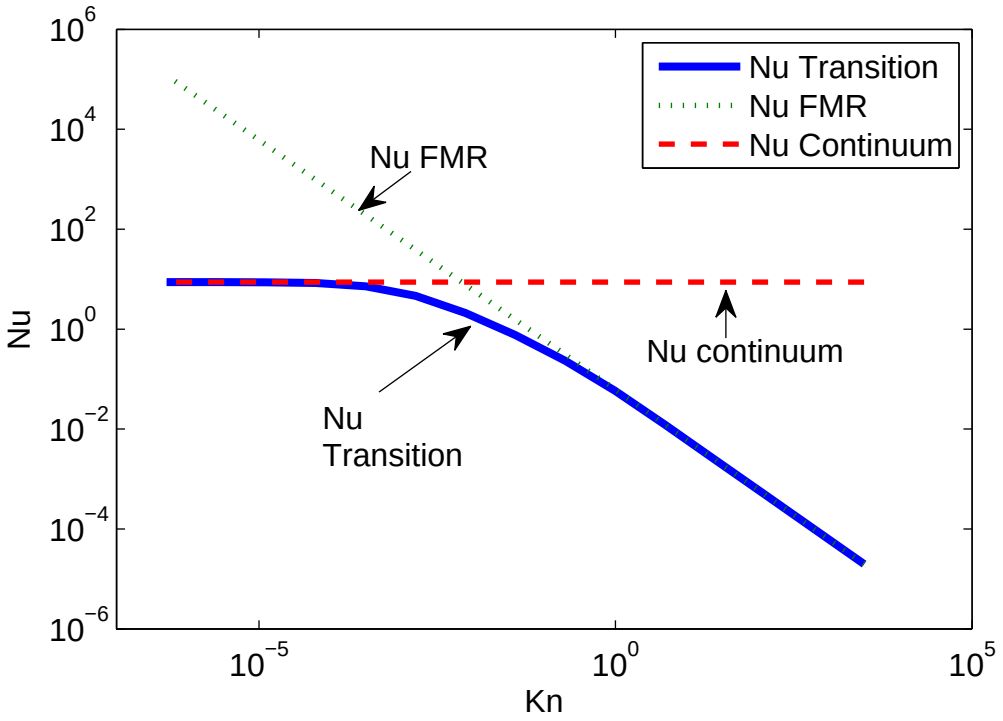

Figure 2.1: Free molecular, continuum, and transition-regime heat transfer from a nanoparticle, as a function of the Knudsen number

model equation is the one developed by Bhatangar, Gross and Krook which is called BGK model [6], and is defined as

$$\frac{\partial}{\partial t}\left(f_v\right) + \mathbf{c}.\frac{\partial}{\partial r}\left(f_v\right) = \nu(f_{v0} - f_v), \tag{2.14}$$

in which f_{v0} is the Maxwell-Boltzmann distribution function for an equilibrium gas and ν is the collision frequency of gas molecules. The collision term in this equation is much simpler than the one in the full Boltzmann equation.

The main assumption in the small perturbation approach is that Knudsen number is either large or small such that the regime is near free molecular or near continuum; in such a case, the Boltzmann equation can be linearized which is easier to solve. This approach is often applied to the BGK model equation [31]. Two studies have been reported in literature where the problem of heat transfer from a spherical particle to the monatomic surrounding gas has been investigated using this approach [11, 44]. Cercignani and Pagani [11] have assumed that the velocity distribution does not deviate significantly from equilibrium Maxwell-Boltzmann equation if the temperature difference between the gas and the particle is small, hence the velocity distribution can be written as

$$\frac{\partial}{\partial t}\left(f_v\right) + \mathbf{c}.\frac{\partial}{\partial r}\left(f_v\right) = \nu(f_{v0} - f_v), \tag{2.15}$$

In the moment method, a specific functional form of velocity distribution which contains many unknown variables is chosen. Then all the terms of the Boltzmann equation are multiplied by a molecular quantity and an integration is performed over the whole velocity space; the resulting expression is a moment equation and this process can be continued to yield higher order moment equations. Since the velocity distribution function is assumed to contain a finite number of macroscopic quantities, the set of equations derived can form a closed set and be solved. Chapman-Enskog theory is a well known example for a mix of moment method with small perturbation approach. A more thorough description of this method can be found in Ref. [7]

2.3.3.2 Interpolation Techniques

Sherman in 1963 [53] proposed a very simple method for estimating heat transfer rate in the transition regime. He reported that, based on experimental observations, the rate of heat transfer in the intermediate transition regime is close to the harmonic mean of the heat transfer in the continuum and free molecular regimes as expressed in the following equation

$$\frac{\dot{q}_{tr}}{\dot{q}_c} = \left(1 + \frac{\dot{q}_c}{\dot{q}_f}\right) \tag{2.16}$$

where $\dot{q}_{tr}$, $\dot{q}_c$ and $\dot{q}_f$ are the transition, continuum and free molecular heat transfer rates respectively. This simple treatment was made more sophisticated later by Fuks, Sutugin and Loyalka [19, 34, 35] assuming complete thermal accommodation

$$\frac{\dot{q}_{tr}}{\dot{q}_c} = \left(1 + Kn\frac{\xi(\dot{q}_c/\dot{q}_f) + \zeta}{\xi Kn + 1}\right)^{-1} \tag{2.17}$$

in which ξ and ζ are non-dimensional coefficients.

2.3.3.3 Two Layer Technique

The most accurate method for modeling transition regime heat transfer is Fuchs's boundary sphere approach [15, 18]. In this model, the gas is divided into two domains separated by a spherical surface called the boundary sphere, located at a radius of $a + \delta$, in which δ is the Knudsen layer thickness, usually chosen to be the same as the mean free path. Molecules are assumed to travel ballistically between the boundary sphere and the particle surface,

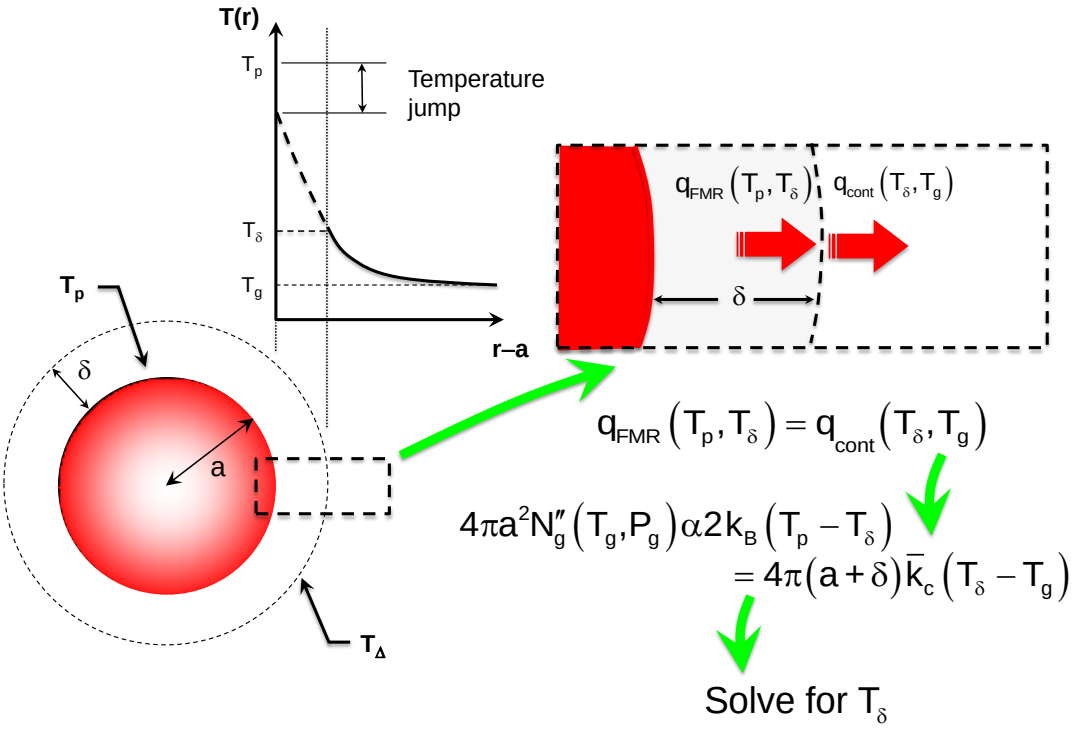

Figure 2.2: An schematic of Fuchs's boundary sphere method

and accordingly heat conduction occurs in the free molecular regime,

$$q_{c,\mathrm{FMR}} = \alpha \pi a^2 \sqrt{\frac{2k_B T_g}{\pi m_g}} \left(\frac{\gamma+1}{\gamma-1}\right)\left(\frac{T_\delta}{T_g} - 1\right) \tag{2.18}$$

Heat transfer between the boundary sphere and the equilibrium gas is assumed to occur in the continuum regime, governed by

$$q_{c,cont} = 4\pi\,(a+\delta)\,\bar{k}\,(T_\delta - T_g) \tag{2.19}$$

where $\bar{k}$ is the average thermal conductivity between T_δ and T_p. Under steady state conditions the heat transfer through the inner free-molecular regime equals that through the continuum regime, resulting in a nonlinear equation

$$4\pi a\bar{k}\left[T_\delta - T_g\right] = \alpha\pi a^2\sqrt{\frac{2k_B T_g}{\pi m_g}}\left(\frac{\gamma+1}{\gamma-1}\right)\left(\frac{T_\delta}{T_g}-1\right) \tag{2.20}$$

that can be solved implicitly for T_δ. Once T_δ is found, the heat transfer rate can be computed accordingly. A schematic of Fuchs's boundary sphere method is shown in Fig. 2.2.

2.3.3.4 Numerical Techniques

The interpolation techniques that neglect the temperature dependence of material properties will be unable to yield reliable results when the ratio of the temperature difference between the gas and the particle to the temperature of the gas ($\Delta T/T_g$) is very large [15]. Other than the analytical methods mentioned before, there can be a numerical approach in modeling heat transfer in LII whose accuracy is not affected by the magnitude of the ratio ($\Delta T/T_g$). Direct Simulation Monte Carlo method (DSMC) is the most successful numerical method for this purpose because it works well for transition and free molecular regime heat transfer in which the Knudsen number is large.

Some researchers have performed steady state DSMC simulations for modeling heat conduction in LII. Filippov and Rosner [15] were the first to model heat transfer between a hot spherical isolated and motionless primary particle and its cold surrounding monatomic gas in transition and free molecular regime using a steady state version of DSMC. The

results of their study shows a good agreement between DSMC and Fuchs two-layer model. Yang et al. [66] later performed the steady state DSMC simulations for a biatomic gas. Two other papers have been published in which the conduction heat transfer rate in free molecular regime is simulated for aggregates [16, 66]. Liu and Smallwood [32] have later modeled the rate of conduction heat transfer between hot fractal aggregates of arbitrary shape and the surrounding gas in the transition regime using a steady state version of DSMC method. They have generated aggregates numerically using cluster-cluster and particle-cluster aggregation algorithms.

The basics of DSMC method were explained in the previous chapter and more details will be discussed in chapter 3 and 4 as necessary. It needs to be mentioned that all of the DSMC simulations previously done in LII are steady state simulations and this study is the first in its kind to investigate the real transient LII process using unsteady DSMC.

2.4 Sublimation in LII

While much work has focused on modeling transient transition regime heat conduction in low fluence LII, the state of sublimation modeling in high fluence LII is still nascent; there remains considerable uncertainty in the underlying physics of sublimation in LII, as evidenced by a significant difference between model predictions and experimental results during the laser pulse and shortly thereafter [41, 54, 51, 57]. Most sublimation models currently used to interpret TiRe-LII data are minor modifications of the original work by Melton [38, 1], who first conceived LII as a soot diagnostic; the state of the art is summarized in [40]. While there have been minor variations and innovations (e.g. modifications

to the mass accommodation coefficient and the molecular mass of sublimed species [54]) all models use the Clausius-Clapeyron model to estimate the number density of sublimed species based on the particle temperature and ambient gas pressure, and all models assume that sublimation occurs in the free molecular regime, which neglects the influence of sublimed species on the gas dynamics surrounding the nanoparticle.

Sublimation becomes important at temperatures around 3800 K [57]. At this temperature gaseous carbon clusters are sublimed from the soot particles; the size of these clusters ranges from C_1 to C_{10}; the most abundant of which is C_3. The rate of sublimation can be found from [54],

$$\left(\frac{dM}{dt}\right)_{evap} = \frac{1}{2}\rho_s \pi d_p^2 \frac{d}{dt}(d_p) = -\pi d_p^2 \beta_{sub} P_v U \tag{2.21}$$

in which d_p is the diameter of the soot particle, ρ_s is the average density of soot and β is the mass accommodation coefficient [32]. The average velocity of the sublimed clusters diffusing from the particle surface, U, is derived from the Maxwell speed distribution defined at the surface temperature T,

$$U = \sqrt{\frac{M_v}{2\pi RT}} \tag{2.22}$$

in which M_v is the mean molecular weight of sublimed species and R is the universal gas constant [57]. The partial pressure of vapor, P_v, is found from the Clausius-Clapeyron equation [25]

$$p_v = p^* \exp\left(\frac{\Delta H_{sub}(T - T^*)}{RTT^*}\right) \tag{2.23}$$

Where p_v is the partial pressure of vapor, p^* and $T^*$are reference temperature and pressure. Using the enthalpy of formation of sublimed carbon clusters, this equation gives the partial pressure of sublimed carbon species as a function of instantaneous temperature of particle

surface during equilibrium phase change from solid to gas state. Sublimation in LII is a strong non-equilibrium process due to extremely large temporal and spatial gradients but there is no better way to estimate the partial pressure of sublimed carbon clusters other than using the Clausius-Clapeyron equation. Using Clausius-Clapeyron equation, Leider et al [27] have developed vapor-pressure data and Michelsen et al [39] have fitted a polynomial to that data. In this study the coefficients in [39] have been used to calculate the partial pressure of sublimed clusters (in this case, only C_3) as a function of the temperature of the particle; using the estimated partial pressure, the sublimation rate is found. In this method of calculating the sublimation rate it is assumed that sublimation is kinetically controlled which means that the transport rate of sublimed clusters does not affect their partial pressure at the vicinity of the particle surface [39]. More details about numerical modeling of sublimation in LII will be provided in Chapter 4.

2.5 Unresolved Issues and Uncertainties in LII

There are several unresolved issues and sources of uncertainty in LII measurements and some of them are discussed in this section. One of these issues which was first mentioned by Snelling et al, in their 2009 paper [57] is the "gas heating"effect. In one of the plots in their paper, the cooling rate versus temperature of soot is shown for different laser fluences. If the soot absorption function, $E(m)$, can be assumed to be independent of soot temperature and the differential cooling of large aggregates can be neglected, then it is expected that the cooling rate for all fluences should become identical at low particle temperatures. This happens for low and medium fluences where the peak soot temperature is moderate but not

for high fluences. At fluences higher than 0.39 mJ/mm^2 they have observed that the cooling rate is lower than the low fluence cooling rate at low soot temperatures. Their conclusion is that at soot concentration of 4-ppm which corresponds to their measurements there can be a significant gas heating effect. They have made an argument about the diffusion speed of heat and concluded that the heat that is absorbed by the soot particles can not scape the beam laser area completely during LII measurements and hence the temperature of the gas in the whole beam area will be higher in case of high fluence LII.

Another phenomenon which remains unexplained to date is an effect called "anomalous cooling". In many LII experiments, pyrometrically-derived temperature decays cannot be explained by steady-state heat conduction models. If the laser-energized particles commence cooling from the same temperature (which is usually a good approximation if the beam fluence is spatially-uniform) a steady-state heat conduction model corresponds to an exponential pyrometric temperature decay at early cooling times, which becomes progressively non-exponential at longer cooling times due to the effect of polydisperse particle sizes [33]. Many researchers, including Daun et al. [12] have observed this effect, i.e. enhanced cooling after the laser pulse, as shown in Fig. 2.3. Other than the discrepancy in the temperature prediction of LII models and pyrometrical measurements, the rate of cooling (loosing sensible energy) at short times after the laser pulse in low fluence LII is about 2 times higher than what the LII models predict. The duration of this anomalous cooling effect is about 50 ns after the peak of laser pulse. Snelling et al, in their 2009 paper [57], have plotted the cooling rate versus $T_{soot} - T_{gas}$ with a very high data precision which can clearly show the anomalous cooling that happens at short times. The cause of anomalous cooling is not very well understood up to now. There are speculations that it may be

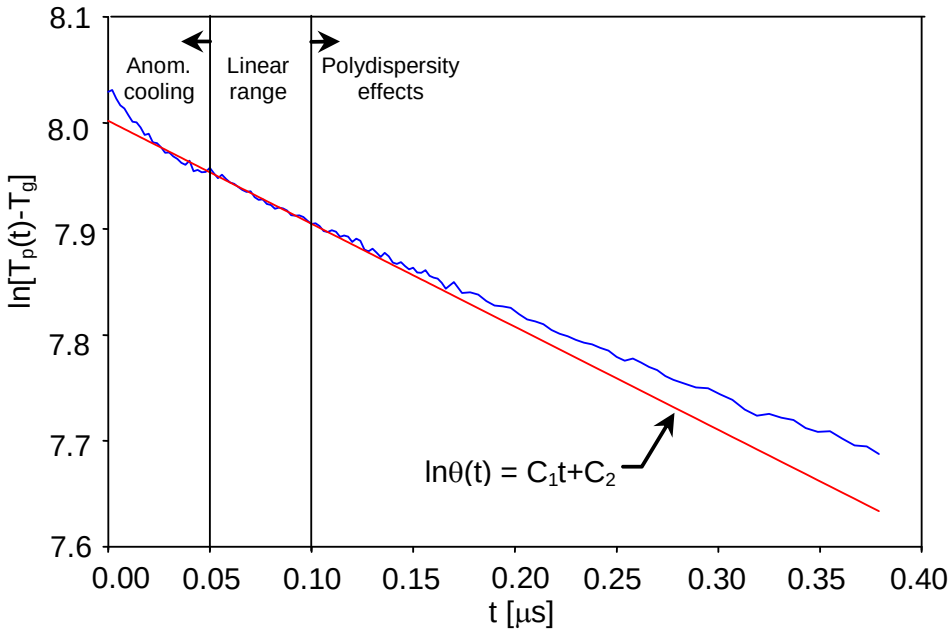

Figure 2.3: Pyrometrically-defined temperature for soot entrained in argon, showing anomalous cooling lasting 50 nm after peak soot temperature [12]

due to evaporation of large polyaromatic hydrocarbons (PAHs) or due to detachment of hydrogen and oxygen atoms from the surface of soot and consequently the conversion of carbon atoms from sp^3 to sp^2 hybridization states [57].

In addition to the above mentioned unresolved issues, there are many sources of uncertainty specific to sublimation. For example: (i) the effect of aggregate shielding on sublimation is unknown; (ii) morphological changes, like soot annealing can affect the sublimation rate significantly; (iii) the entropy and enthalpy of evaporation and the mass accommodation coefficient used to calculate the sublimation rate of soot have been de-

rived from experiments on bulk graphite surfaces, which may not be representative of soot properties; (iv) non-thermal photo-desorption during the pulse may contribute to sublimation/evaporation [41, 40]. Perhaps most glaringly, however, is that the influence of the sublimed species on the gas dynamics surrounding the particle has been ignored. Implicitly, Eq. (2.21) assumes that the sublimed species leave the primary particle in the free molecular regime, with a molecular flux characteristic of an equilibrium gas at T_p. This state-of-affairs is remarkable, considering the extensive development of transition-regime conduction models for LII experiments carried out on larger monomers or aggregates, or in high-pressure aerosols. The nature of heat conduction depends on the Knudsen number, $Kn = L_{MFP}/d_{eff}$, where L_{MFP} is the mean free molecular path in the gas and d_{eff} is a characteristic length; either the diameter of a monomer, or some effective diameter in the case of an aggregate. When Kn is large it is reasonable to assume free molecular diffusion, i.e. that the gas molecules travel ballistically between the particle surface and the equilibrium gas. When Kn approaches unity, however, this assumption is no longer valid since intermolecular collisions in the vicinity of the particle surface will influence the local gas properties [24]. There has been some speculation in the literature that collisions involving sublimed carbon clusters may influence the gas dynamics, e.g. the possibility of shock waves [41], and that the sublimed species may return to the particle surface via intermolecular collisions with other sublimed clusters and the bath gas [57].

The purpose of this thesis is to investigate some of the unresolved issues in low fluence and high fluence LII. In low flucence LII, one of the possible causes of anomalous cooling which is the transient heat conduction effects is investigated (Chapter 3). Every model of heat conduction in LII works based on steady state conditions assumption, but in reality,

heat conduction in LII is highly unsteady and there are very large temporal gradients of quantities like temperature, pressure, number density and etc.

In high fluence LII, the back flow of sublimed species and formation of shock waves is studied (Chapter 4). The numerical tool used for both issues is transient Direct Simulation Monte Carlo method [7].

Chapter 3

Transient Transition Regime Heat Conduction in LII

3.1 Introduction

In this chapter the transient transition regime heat conduction is modeled using DSMC. First the importance of transient effects is analytically analyzed and then the details of the DSMC simulation is explained. The results and their impact on clarifying the causes of some unresolved phenomena are discussed at the end of the chapter.

3.2 Analytical Evaluation of the Importance of Transient Effects

The applicability of a steady-state transition regime heat conduction model can be investigated by comparing the characteristic cooling time of the particle to the characteristic response time of the gas, following Filippov and Rosner [15]. It is proposed in Ref [15] that, in case of a monomer in the transition regime, the response time of the gas can be estimated as

$$\tau_{eq} = \frac{a}{\bar{c}} \tag{3.1}$$

where $\bar{c}$ is the mean thermal speed of the gas. Eq. (3.1) is based on the argument that $Kn = \lambda_{MFP}/a \sim O(1)$ and gas molecules must undergo several collisions [57], therefore traveling several mean free paths, to reach an equilibrium distribution.

To find the characteristic time of particle temperature change in the transition regime, the free molecular heat transfer rate is equated to the rate of sensible energy loss

$$m_p c_p \frac{dT}{dt} = \alpha \pi a^2 n_g \bar{c} k_{\mathrm{B}} \left(2 + \frac{\xi_{int}}{2}\right) (T_p - T_g) \tag{3.2}$$

Non-dimensionalizing temperature by $\theta^* = (T - T_g)/(T_p - T_g)$ and time by $t^* = t/\tau_{p,h}$, where $\tau_{p,h}$, is the characteristic cooling time of the monomer, results in $dT/dt \sim (T_p - T_g)/T_{p,h}$, since

$$\left[\frac{d\theta^*}{dt^*}\right] \sim O(1) \tag{3.3}$$

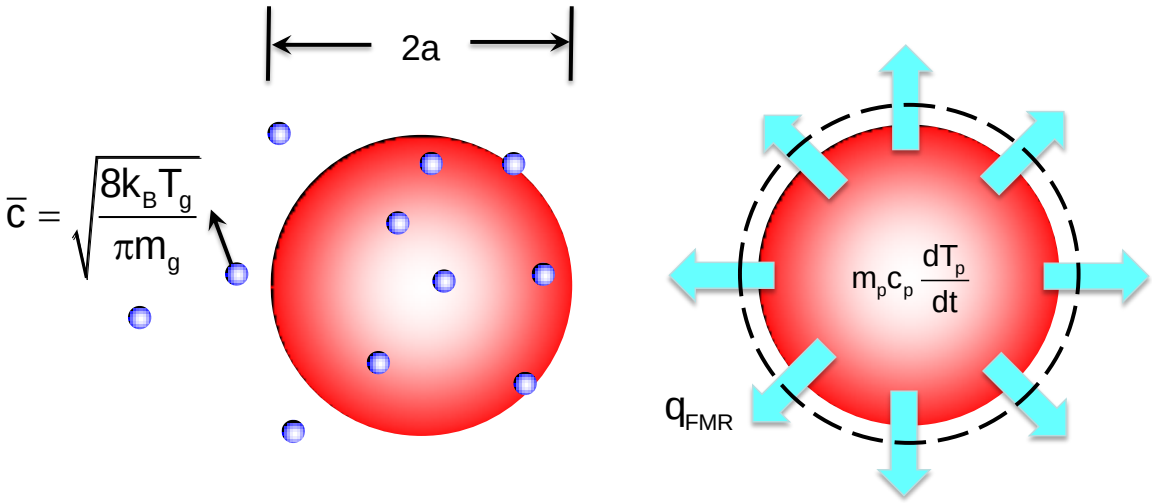

Figure 3.1: Length scales in analytical analysis of the importance of transient effects

Finally, for a monatomic molecule like argon, $\xi_{int} = 0$, so

$$\tau_{p,h} = \frac{m_p c_p T_g}{2\alpha\pi a^2 p_g \bar{c}} \tag{3.4}$$

The ratio of these two characteristic times gives

$$\frac{\tau_{p,h}}{\tau_{eq}} = \frac{\rho_p c_p m_g T_g}{2\alpha\rho_g k_B} \tag{3.5}$$

which must be much greater than unity for the quasi-steady state treatment to be valid. This condition is usually satisfied for a primary particle because the density of graphitic soot is much higher than that of the gas while $c_p m_g / k_B \sim O(1)$. While the quasi-steady state assumption is usually valid for dense spherical particles and aggregates, this may not be the case for sparse aggregates. In this scenario, the characteristic response time of the

gas is defined using the geometric length of the aggregate, L, hence

$$\tau_{eq} = \frac{L}{\bar{c}} \tag{3.6}$$

Equating the heat transfer rate of free molecular regime to the rate of sensible energy loss results in

$$\frac{4}{3}\pi a_p^3 \rho_p N c_p \frac{dT}{dt} = \alpha \pi a_{eq}^2 n_g \bar{c} k_{\mathrm{B}} \left(2 + \frac{\xi_{int}}{2}\right)(T_p - T_g) \tag{3.7}$$

where a_{eq} is the equivalent heat transfer radius of the aggregate, N is the number of primary particles in an aggregate, and c_p is the specific heat of soot. Using the same non-dimensionalization described above, Eq. 3.7 simplifies to

$$\tau_{p,h} = \frac{a_p^3 \rho_p N c_p}{{a_{eq}}^2 \bar{c}} \frac{m_g}{k_B \rho_g} \tag{3.8}$$

By definition it is known that

$$\eta_{sh} = \frac{4\pi a_{eq}^2}{4\pi a_p^2 N} \tag{3.9}$$

in which η_{sh} is the shielding coefficient, which accounts for the fact that primary particles near the aggregate interior are not entirely accessible to incident gas molecules due to primary particle on the exterior. Typically $\eta_{sh} \sim O(1)$ so $a_{eq}^2 \sim a_p^2 N$, and consequently

$$\tau_{p,h} = \frac{a_p \rho_p c_p}{\bar{c}} \frac{m_g}{k_B \rho_g} \tag{3.10}$$

and

$$\frac{\tau_{p,h}}{\tau_{eq}} = \frac{\rho_p c_p m_g a_p}{k_B \rho_g L} \tag{3.11}$$

The case corresponding to the data shown in Fig. 2.3 is considered, in which LII measurements were made on soot generated by a laminar diffusion flame and then entrained into argon at 293 K and 1 atm [12]. To find the ratio of the characteristic times, L is estimated to be the same as the equivalent sphere diameter, D_{eq}, which is given by the fractal-relationship (3.12)

$$D_{eq} = d_p(N_p/f_a)^{(1/2\varepsilon_a)} \tag{3.12}$$

where d_p is the diameter of a primary particle and N_p is the number of primary particles in the aggregate, taken to be 29.7 nm and 184, respectively, based on a TEM study of extracted soot aggregates [12]. The fractal prefactor, f_a, and fractal exponent, ϵ_a are given by

$$f_a = 1.04476 + 0.22329\alpha + 7.14286 \times 10^{-3}\alpha^2 \tag{3.13}$$

and

$$2\varepsilon_a = 1.99345 + 0.30224\alpha - 0.11276\alpha^2 \tag{3.14}$$

based on a Monte Carlo simulation done in the free-molecular regime [33]. In this research the thermal accommodation coefficient is taken to be 0.35, representative of the values used in other DSMC studies of transition-regime heat conduction [15, 31, 18]. This value was chosen based on the linear regression like what is shown in Figure 2.3, only the part between 50 ns and 100 ns was considered, the data for times smaller than 50 ns and specially smaller than 25 ns cannot be considered because there is a non exponential trend in that part and the accommodation coefficient is only meant to model gas surface scattering interaction not any other mechanism of energy transfer. These calculations result in an equivalent sphere diameter of 342 nm. This diameter is related to the aggregate shielding parameter

in Eq. 3.9 by

$$D_{eq} = \sqrt{\eta_{sh} D_p^2 N} \tag{3.15}$$

Substituting in these parameters, and typical constant values for $\rho_p = 2100\,\mathrm{kg/m^3}$ [12] and $c_p = 1900\,\mathrm{J/kg.K}$ [40] for soot results in $\tau_{p,h} = 450$ ns and $\tau_{eq} = 0.868$ ns, and $\tau_{p,h}/\tau_{eq} = 507$. While this result suggests that the quasi-steady state approach may be reasonable under these conditions, because the sampling frequency in LII experiments is often of the order of 1 ns, temperatures measured shortly after the pulse may not, in fact, satisfy conditions for quasi-steady state heat conduction. DSMC results in this chapter will show that there is a distinct transient effect and the steady state models can not capture it. At the end of this chapter there will also be a discussion about defining a better characteristic equilibrium time.

3.3 Transient DSMC in Modeling Conduction Heat Transfer

The basics of DSMC method were explained in the previous chapter with a focus on steady state DSMC. This is the first study that is using a transient DSMC simulation for modeling transient conduction during LII.

Transient DSMC method has been used to investigate whether the quasi-steady state approach is appropriate for LII models. The results of transient DSMC simulation have been compared to steady state DSMC and Fuchs' method to evaluate the importance of transient heat conduction effects.

3.3.1 Computational Domain

The computational domain used in this study is shown in Fig. 3.2. Due to the extreme computational expense of DSMC simulations, the outer domain cannot extend to the equilibrium gas. In this study, the computational domain reaches a radius of 3 μm, representing the average half-distance between aggregates for soot loadings typical of an ambient flame [57]. Steady state DSMC simulations [15, 31, 32] have defined this boundary condition using a variation of Fuchs's boundary sphere method, in which the outer boundary temperature is updated throughout the simulation by matching the DSMC-derived instantaneous heat conduction rate to a steady-state continuum solution between the outer domain surface and the equilibrium gas. This treatment is inapplicable to transient heat conduction simulations, so the outer domain temperature is simply set equal to 293 K, with the understanding that this boundary condition is valid only for short cooling times. Based on a continuum analysis, it takes more than 100 ns for the thermal wave to reach the boundaries so if the domain radius is 3 μm and its temperature is 293 K, this will not cause any error in any of the simulations before 100 ns.

3.3.2 Modeling the Surrounding Gas

The surrounding gas has been chosen to be argon for simplicity. Argon is a monatomic gas and can be accurately modeled as a hard sphere gas in which the heat conductivity coefficient obeys a power law, $k(T) = k_{ref}(T/T_{ref})^{\omega}$, with $\omega = 1/2$. In this model the collision cross section is independent of relative velocity of the colliding molecules and an isotropic scattering is considered in the center of mass frame of reference. Hard sphere

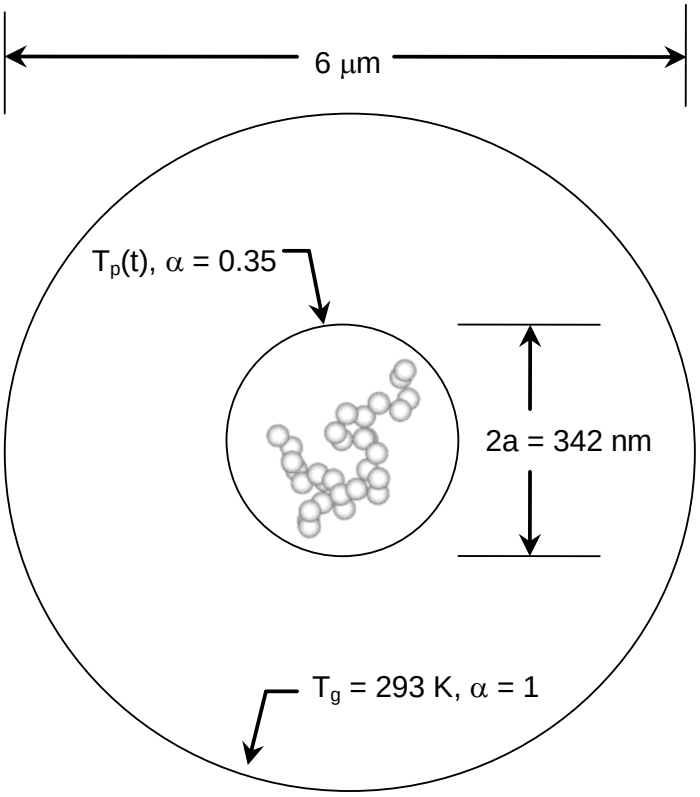

Figure 3.2: DSMC Simulation geometry (not to scale).

model only considers the translational energy of molecules and neglects their rotational and vibrational energy which works well for monatomic molecules which do not posses any internal energy of rotational or vibrational form.

3.3.3 Modeling Soot Nano-particles

Rather than model the aggregate structure in detail (which to date remains computationally intractable in the transition regime [41]) the equivalent sphere defined in Eq. (3.12) has been used. Substituting Eqs. (3.13) and (3.14) into Eq. (3.12) results in an effective diameter of 342 nm. The inner surface of the computational domain is the surface of the equivalent sphere.

3.3.4 Surface Interaction Model

The collision between the gas molecules and the surface of the particle at the inner surface of the computational domain is modeled by classical Maxwell model [7] which is an idealization and as was discussed in Chapter 2, the true scattering behavior is governed by a scattering Kernel. In Maxwell model, any collision between the molecules and the particle surface is either considered to be specular or diffuse on a probabilistic basis. It is the thermal accommodation coefficient, α, which determines the probability of each collision type. If the accommodation coefficient is 1, all the collisions are considered to be diffuse, and if it is zero, all the collisions are treated as specular reflection. In general the probability of diffuse reflection is α and that of specular reflection is $(1 - \alpha)$.

If a collision is chosen to be diffuse, the post collision velocity of the incident molecule will be determined from a half Maxwellian equilibrium distribution at the instantaneous particle temperature and will be completely independent of the incident velocity. If the collision is specular, on the other hand, there is no energy transfer of any type between the particle surface and the gas molecule and the post collision velocity will not be affected

by the temperature of the surface but will only reverse its normal component of velocity, and the other velocity components will remain intact. The energy transfer in each diffuse reflection is calculated by comparing the energy of molecules before and after the collision and the heat conduction rate is calculated by summing these individual energy transfers and dividing by the corresponding time. Since a single time step is a very short time and the number of molecule-surface interactions is very small in each time step, the heat transfer rate is calculated after each 1 ns; since the temperature of the particle does not change significantly in 1 ns, it still gives a good temporal resolution of the change of heat transfer rate by time.

The Maxwell model of molecule-surface interaction is implemented in DSMC code as follows. In each time step, the trajectory of individual molecules is calculated deterministically based on their last stored velocity and position for the duration of a single time step by neglecting any solid boundary. If the calculated end position of the molecule is such that it requires crossing a solid surface, a collision is considered to happen and the fraction of time step before and after the collision is calculated. Then in order to determine whether the collision is diffuse or specular, a uniformly distributed random number between 0 and 1, $R(f)$ is generated. If this number is larger than α, the collision is assumed to be diffuse and otherwise is it treated as specular.

The particle temperature is updated at the beginning of each time step according to a polynomial expression, $T_p(t)$, fit to pyrometrically-inferred experimental data from [57], shown in Fig. 3.3.

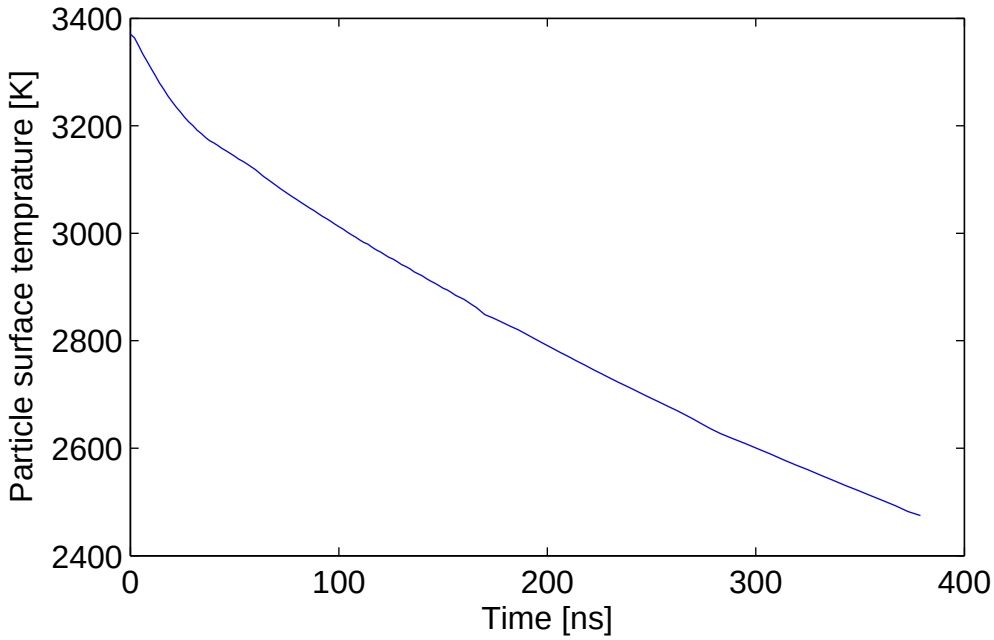

Figure 3.3: Particle temperature decay curve, based on pyrometrically-derived temperatures from [12]

3.3.5 Discretization of the Computational Domain

Now that the computational domain is defined, it should be discretized using a number of cells. There are a number of issues to consider in choosing the cell size. If the cell size is chosen to be very large, the DSMC simulation will be unable to capture steep gradients in temperature, pressure and other properties. The smaller the size of the computational cells, the more accurate the DSMC simulation will be. For matters of statistical stability, it is recommended for each computational cell to contain no less than 20 simulated molecules, and if the number of cells is very large, then the number of simulated molecules will also increase accordingly; the computational time in NTC method which is used here, is proportional to the total number of simulated molecules in the flow field and hence the

computational time will also increase which is undesirable. It is recommended that the cell size be no more than 1/3 of the expected mean free path [7]; based on this criterion, in this study, the 1D radial geometry is discretized into 150 equal cells. It should be noted that the cell size is the same only in the radial direction, each cell is a spherical shell and different cells have different volumes and the further away they are from the particle surface the larger they are.

3.3.6 Initial Conditions

Based on the requirements for minimum number of simulated molecules in each cell, the gas is initially represented using 10^6 simulated molecules, each one representing 2700 real molecules.

In any DSMC simulation, the initial condition must be specified. When a steady state DSMC simulation is being performed, the initial condition is arbitrary as long as the boundary conditions are properly defined, since the simulation will change to the steady state solution. But in case of transient DSMC, the initial condition specified in the code must exactly match the physical problem. In case of the simulation done in this study, the initial condition is defined as argon in atmospheric pressure and at temperature of 293 K; based on this initial condition and using the ideal gas law, the number density of the gas is determined and since the size of the flow field is also known, the number of real molecules can be evaluated. Once the number of real molecules in the flow field is calculated, by dividing that number with the number of simulated molecules, the number of real molecules represented by each simulated molecules will be determined which in this

case is 2700.

3.3.7 Time Step

After discretization of the domain, an appropriate time step must be chosen. When a transient DSMC simulation is being performed, the time step actually corresponds to the passage of real time. Like the cell size, the smaller the time step the more accurate the simulation. There are several criteria for choosing the time step; the molecules on average should not travel a distance larger than cell dimension over a single time step; and the time step should be only a fraction of the mean collision time. Based on these criteria, the time step in the current calculations is chosen to be 10^{-11} s which corresponds to 4% of the mean collision time. In this transient simulation, time steps correspond to the passage of physical time, i.e. when one time step passes, it is equivalent to 10^{-11} s of the real transient process.

3.3.8 Sampling Thermodynamic Properties

While both ensemble and time averaging can be used to reduce variance in steady-state DSMC, in transient DSMC only ensemble averaging is used. There is no time-averaging except for the heat transfer rate, which is calculated by aggregating the kinetic energy change of molecules scattering from the particle surface over each time step. To further reduce the sample variance, the simulation needs to be replicated over and over again with a new random seed to yield a large sample size for each cell at each time until the variance of the problem becomes sufficiently small.

Both steady state and transient DSMC simulations model the transient evolution of the flow field from the chosen initial condition to the steady state, but steady state simulations disregard samples collected at the transient phase; any data that is collected after the transition phase can be used to reduce variance in the properties of the flow field for the steady state. In transient DSMC, it is not practical to store the information at the end of each time step. Instead, certain points of time must be chosen at the designated of the simulation and only the information for those points of time is sampled. In fact at each one of those selected points of time the information in every cell is sampled and each time the simulation is replicated and reaches that certain point of time, the sample size at that time will increase.

3.4 Results

Figure 3.4 compares instantaneous gas temperatures obtained from transient and steady state DSMC simulations at 0.1 ns, 0.3 ns, 0.7 ns and 1 ns after the peak soot temperature. The steady state curves are almost identical because the temperature of the particle does not change significantly over 1 ns, but the transient curves change dramatically as the gas responds to the particle temperature. This result highlights the finite response time of the gas to the laser-energized pulse. In fact, the temperature of the surface of the particle is applied as the boundary condition. The gas layer adjacent to the surface feels this boundary condition almost immediately but it takes some time for this information to propagate to the rest of the flow field. The scale analysis done by Filippov and Rosner which was discussed at the beginning of this chapter predicted no important transient

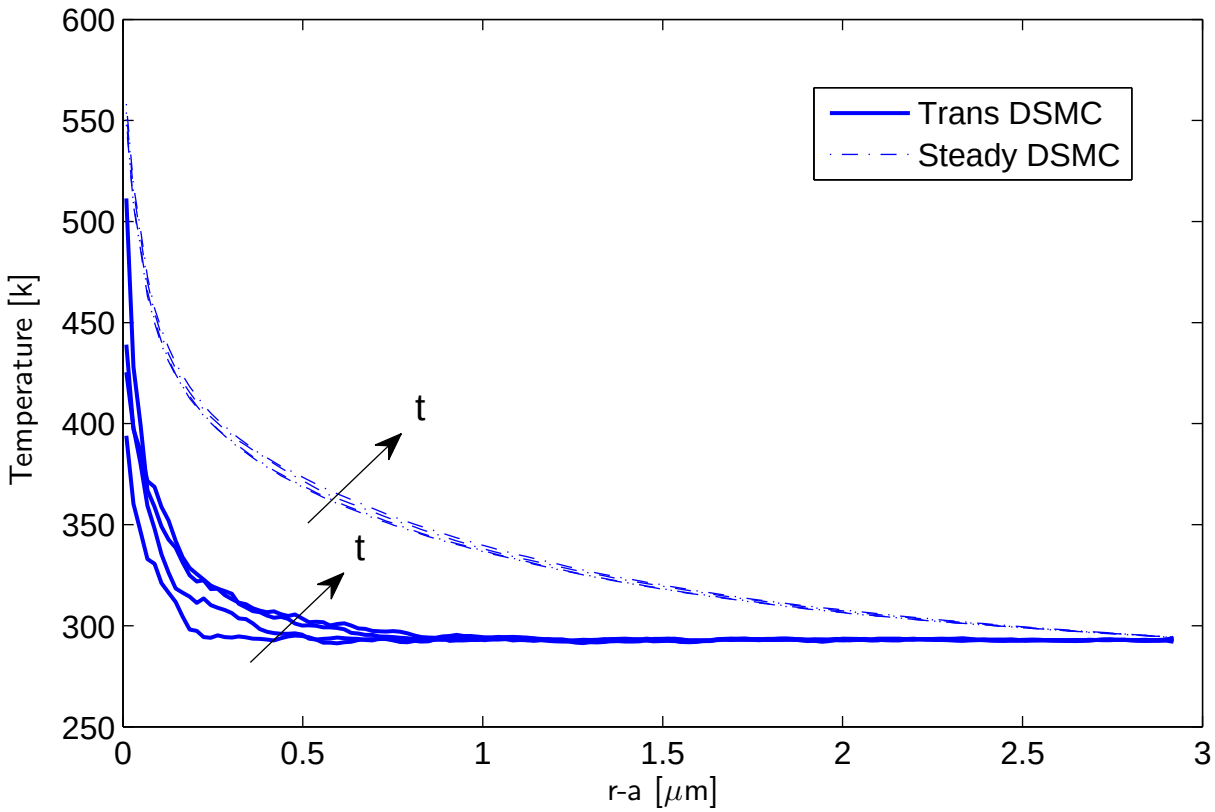

Figure 3.4: DSMC modeled gas temperatures at 0.1, 0.3, 0.7, and 1 ns after the laser pulse

effects but Figure 3.4 shows otherwise.

The impact of this finite response time on the heat transfer rate is shown in Fig 3.5. The transient DSMC model predicts a greater heat transfer rate at shorter times, but approaches the cooling rate predicted using the steady state model after approximately 50 nanoseconds, which appears to match the duration of anomalous cooling shown in Fig. 2.3. The scale analysis proposed by Filippov and Rosner is again unable to predict this period of 50 ns but another scale analysis will be discussed at the end of this chapter which

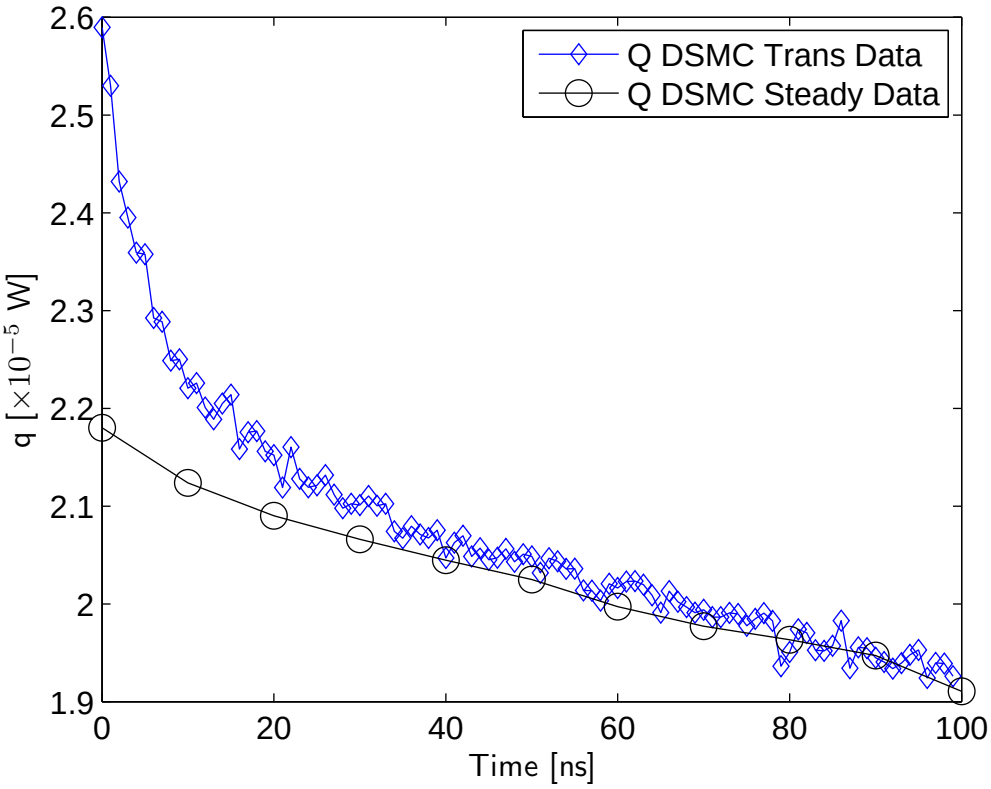

Figure 3.5: Heat transfer from laser-energized particles, modeled using transient and steady-state DSMC techniques

is more successful in predicting this transient response.

The authur's speculation is that one of the causes of this enhanced cooling after the laser pulse is the non-stationary nature of the gas at short time periods. Figure 3.6 shows how the number density of the gas changes with time. Initially the number density of the gas is uniform at $n_g = P_g/(k_B T_g)$, but it drops as the gas adjacent to the particle surface heats up, causing a molecular flux away from the particle surface. This, in turn, causes the initial number flux on the particle surface to be larger than the steady state value of

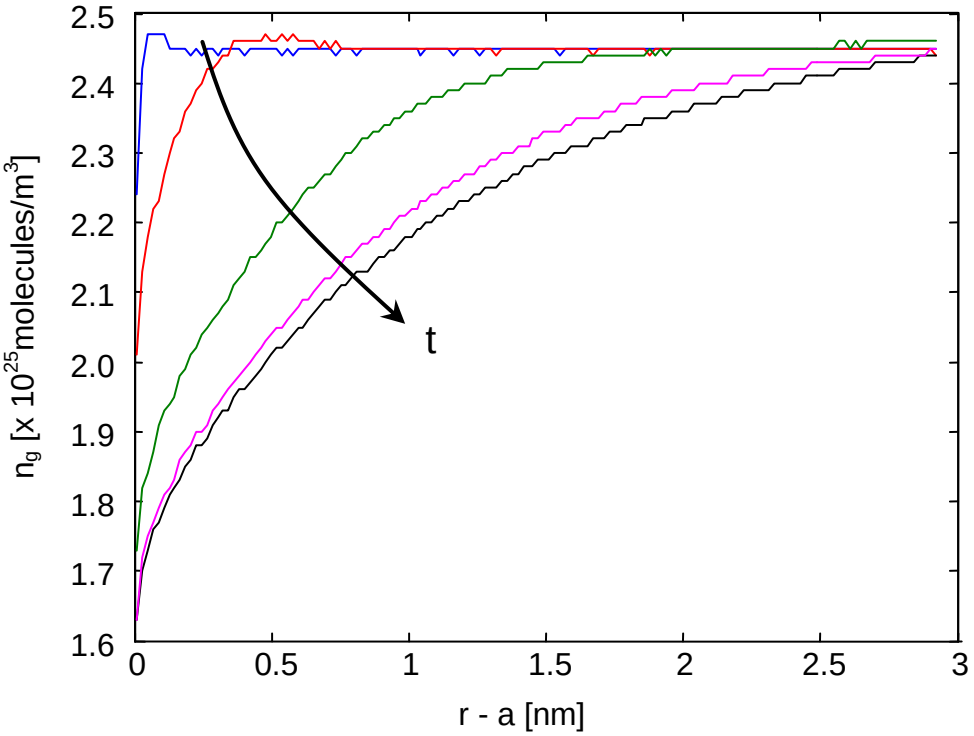

Figure 3.6: Number density in the gas plotted at 0.1, 1, 10, 50, and 100 ns after peak particle temperature.

$N'' = n_g c_g/4$ for a stationary gas.

The relationship between enhanced transient cooling due to the nonstationary gas predicted by DSMC and the experimentally-observed anomalous cooling shown in Fig. 2.3 is further investigated by calculating the conduction heat transfer from the decay in sensible energy inferred from the pyrometrically-derived temperatures,

$$q_c = \frac{4}{3}\pi a^3 \rho\left(T_p\right) c_p\left(T_p\right) \frac{dT_p}{dt} \tag{3.16}$$

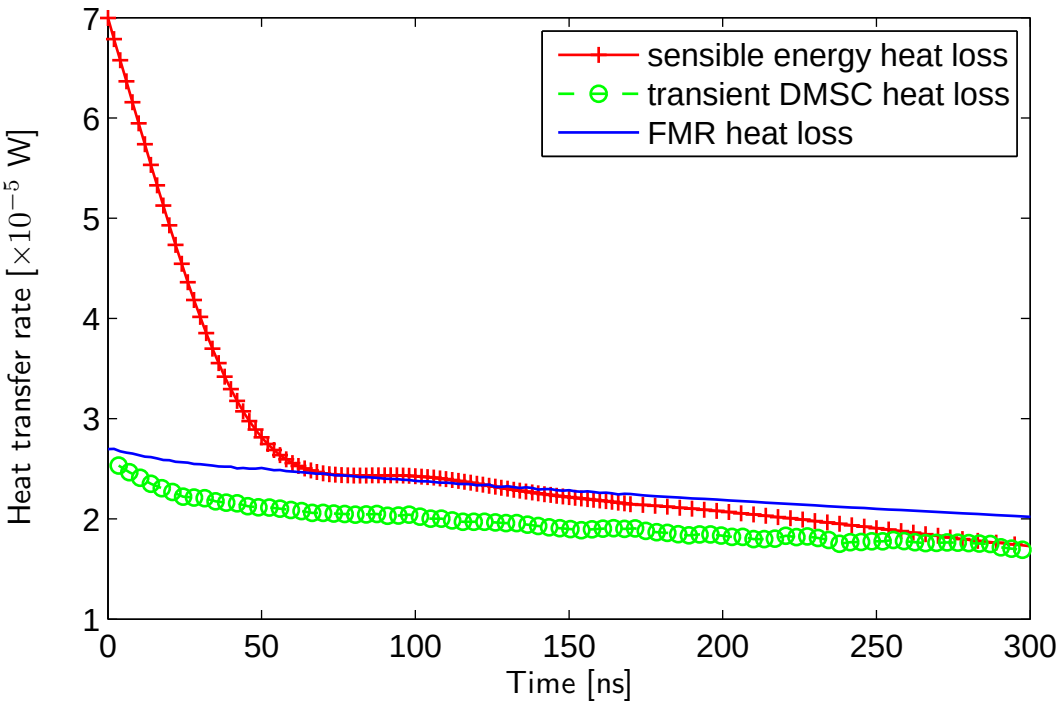

Figure 3.7: Comparison of heat transfer rates derived from DSMC, sensible heat loss and free molecular equation

where constant values of $\rho(T) = 2100$ kg/m^3 and $c_p(T) = 1900$ J/kg.K are used from Ref. [42]. Both the density and specific heat coefficient are functions of temperature but in this study an average value is used for simplicity. The temperature gradient is estimated using forward finite differences, with Tikhonov regularization to stabilize against noise amplification [21, 5, 65].

Figure 3.7 compares the heat transfer predicted by Eq. (3.16) to the values obtained from transient DSMC simulation and the free molecular heat transfer. It is evident that at small times, i.e. below 50 ns, the heat transfer curve derived from the sensible energy loss is much higher than that caused by the transient response of the gas. This result suggests

that the non-stationary gas by itself is insufficient to explain the experimentally-observed anomalous cooling rates, and some as yet unidentified phenomenon must be responsible for the majority of anomalous cooling.

3.5 Conclusions

Transient DSMC simulations has been used to investigate different transient conduction effects that may happen during the LII process. Comparing the temperature curves calculated using transient and steady state DSMC at different times in the cooling process clearly shows the finite response time of the gas to an abrupt change in the particle temperature caused by the laser pulse. The transient gas response causes increased cooling compared to the steady state prediction, lasting up to approximately 50 ns after the laser pulse. This is due to a flow of molecules away from the particle as the gas becomes stationary. Nevertheless, a comparison of the heat transfer rate predicted by transient DSMC to the heat transfer inferred from the measured pyrometric temperature decay shows that, while a small percentage of anomalous cooling is due to transient gas dynamics, an as-yet unidentified phenomena is responsible for the majority of anomalous cooling. A strong candidate for this effect is prompt evaporation of volatile desorbed species from the particle surface [57].

In order to have a more realistic simulation for this problem, we plan to change the particle temperature based on the instantaneous heat transfer rate from the particle instead of using a predetermined temperature curve. In this study, argon has been used as the surrounding gas, but a more realistic choice can be made by using the real products of

combustion instead of argon.

The author believes that the definition of the equilibrium characteristic time in [15] is not realistic. The equilibrium characteristic time should not be so heavily dependent of the size of the particles. Using the definition of Fourier number, $Fo = \alpha_d t/L_c^2$, another definition for the equilibrium time can be proposed. Fourier number will be ~ 1 if t in the definition of Fo number is substituted by τ_c, hence the characteristic time can be defined as

$$\tau_c = \frac{L_c^2}{\alpha_d} \tag{3.17}$$

where α_d is the thermal diffusivity coefficient defined by

$$\alpha_d = \frac{k_g}{\rho_g C_{p,g}} \tag{3.18}$$

in which k_g is the thermal conductivity coefficient of the gas, ρ_g is the density of the gas and $C_{p,g}$ is the specific heat of the gas. All of these three properties are dependent on temperature which changes both temporally and spatially in case of particle cooling during LII. The thermal conductivity of argon at atmospheric conditions which is the same as the ambient gas conditions used in this study is 0.017 $\mathrm{Wm^{-1}K^{-1}}$ [28, 63], the density is 1.603 $\mathrm{kg.m^{-3}}$ and $C_{p,g}$ and the specific heat, is 521.5 $\mathrm{J.kg^{-1}.K^{-1}}$ [29]. Based on these values, α_d is calculated to be 2.11731E-05 $\mathrm{m^2/s}$. The characteristic length in equation (3.17) could be defined as a distance that the thermal wave needs to propagate in order for the transient solution to be close to the steady state solution. The continuum heat transfer rate at any

radius in the gas could be expressed as

$$q_r = 4\pi r^2 k \frac{\mathrm{d}T}{\mathrm{d}r} = const \tag{3.19}$$

which in case of steady state conduction is

$$q_r = 4\pi(a+\delta)k(T_\delta - T_g) \tag{3.20}$$

Equating equations (3.19), (3.20) and non dimentionalizing temperature by

$$\theta = \frac{T - T_g}{T_\delta - T_g} \tag{3.21}$$

gives

$$a + \delta = -r^2 \frac{\mathrm{d}\theta}{\mathrm{d}r} \tag{3.22}$$

which after performing the integration simplifies to

$$\theta = \frac{a+\delta}{r} \tag{3.23}$$

If the criterion for the characteristic length is that the thermal wave must reach a distance where the temperature difference relative to the ambient temperature is 1/10 of its value at the boundary layer, then θ would be 0.1 and for an aggregate radius of 100 nm and a δ of approximately 100 nm, it gives a characteristic length of 2 μm. Using this length in equation (3.17) gives the characteristic time of 188 ns which is a much better approximation of the response time of the gas to the initial temperature rise of the particle.

This treatment is much more realistic than the Filippov and Rosner scale analysis. They were trying to find a characteristic equilibrium time while what matters in this case, is the characteristic response time of the gas to transient effects which can be called the "characteristic steady state response time of gas" which is the time it takes for gas to reach steady state if the boundary condition is kept constant. In fact, physics of LII is a strong non-equilibrium situation. The gas is never in equilibrium even if it could be assumed to be in steady state. In order to have equilibrium, there should be no temporal or spatial gradient, while in the heat transfer problem that takes place in LII both gradients exist. The proposed scale analysis in this study is based on the logic of estimating the time it takes to reach steady state and hence is more realistic.

Chapter 4

Sublimation in High Fluence LII

4.1 Introduction

In this chapter, sublimation in LII is modeled using transient DSMC method to address some of the unresolved issues, namely back flux of sublimed species and shock waves. The computational parameters of the DSMC code used are explained and the collision models used are discussed. At the end of the chapter the results are presented and the new finding about the back flux of sublimed species is discussed.

4.2 Problem Description

Following previous DSMC studies, two scenarios are considered: (1) an isolated primary particle having a diameter of 29.7 nm, and (2) a soot aggregate containing 184 primary particles based on a TEM study of extracted soot aggregates [61, 60, 12]. The reason why

these two cases are considered is to isolate the role that intermolecular collisions play in the gas dynamics of sublimed species. Like the previous chapter, instead of modeling the aggregate structure in detail (which is computationally-intractable in the transition regime [41]) the equivalent sphere diameter, D_{eq}, defined in Eq. (3.12) has been used. It should be noted that Eqs. (3.13) and (3.14) were derived considering aggregate structural shielding under free-molecular conditions, and do not directly apply to sublimation. Since no relationship has been suggested in literature for calculating the equivalent sphere diameter of a subliming aggregate, this value has been used as an estimate of the effective size of the aggregate relative to the mean free molecular path in the gas. Thus, any differences between the case of an isolated primary particle and the larger sphere can be attributed to intermolecular collisions in the particle's vicinity.

4.2.1 Computational Domain and Other DSMC Parameters

Figure 3.2 shows the computational domain for an aggregate (The same domain is used for modeling sublimation from a single primary particle by adjusting the diameter of the inner sphere to be equal to that of a primary particle.) The cell size is chosen to be smaller than 1/3 of the expected mean free path. Based on this criterion, the 1D radial geometry is discretized into 150 equally-spaced cells [33]. The particle is immersed in nitrogen at $T_g = 1900\,\mathrm{K}$ and $P_g = 1\,\mathrm{atm}$, representative of flame conditions. Now that the cell size is determined, the time step is chosen to be $10^{-11}\,\mathrm{s}$ based on the criteria mentioned before in section 3.3.

A thermal accommodation coefficient of 0.35 is prescribed to model energy transfer

between both N_2 and the sublimed clusters and the surface; this value is representative of the values used in other DSMC studies of transition-regime heat conduction [25, 27]. The inner domain of the flowfield conforms to the surface of the equivalent sphere or single primary particle. While the outer domain would ideally extend to the equilibrium gas, such a simulation would be computationally-intractable. Accordingly the outer extent of the computational domain used in this study is $3\,\mu$m, which is half of the average distance between soot particles for typical soot loading in a coflow ethene diffusion flame [57] as was discussed before in section 3.3.1. (This treatment is only reasonable at short times after the pulse, before the inner surface boundary condition has propagated through the domain).

4.2.2 Boundary Conditions

The time varying surface temperature of the particle/aggregate is incorporated as a boundary condition in the DSMC code. At the present time, pyrometrically-derived experimental temperatures that include the laser pulse which is central to the present discussion are not available. Instead, Fig. 4.1 shows the two simulated temperature decay curves considered in this study: one corresponding to a higher fluence condition (0.436 J/cm^2) and the other a lower fluence (0.16 J/cm^2.) These curves were derived under conditions typical of a coflow ethene diffusion flame [41].

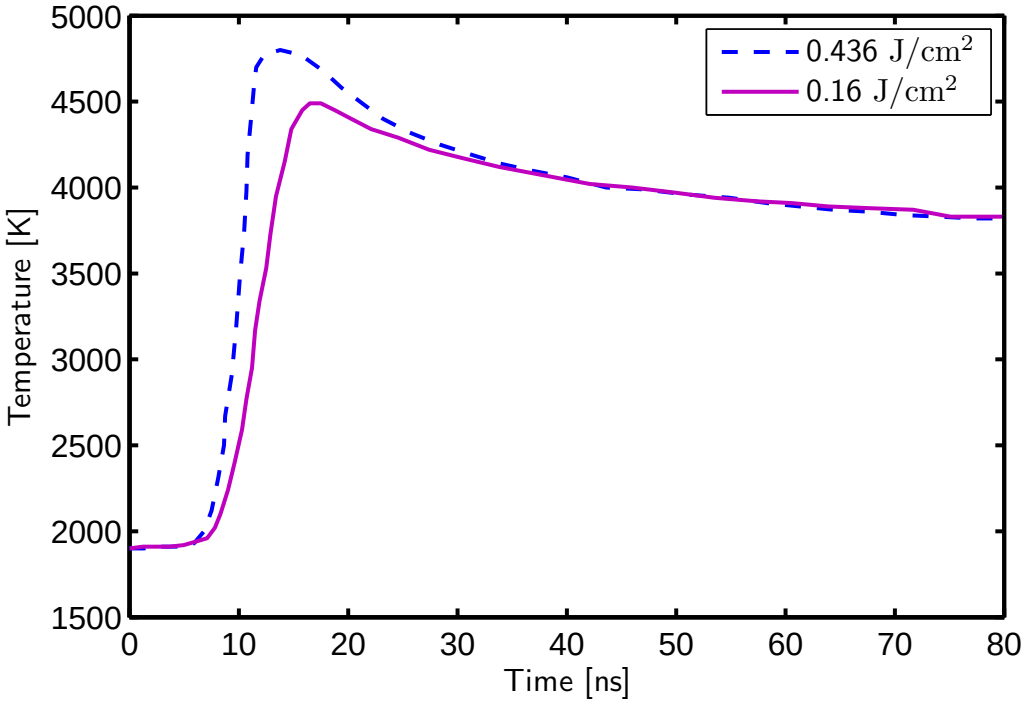

Figure 4.1: Effective modeled temperatures at two different fluences [41]

4.2.3 Subliming Species

As mentioned before, graphite begins to sublime at temperatures higher than 3800 K; producing carbon clusters ranging from C_1 to C_{10}, the most abundant carbon cluster in graphite vapor is C_3 in the temperature range of interest [54] as the thermodynamic equilibrium calculations performed by Leider et al. [27] confirm. Many of the sublimation models presented in [51] have also assumed that the only subliming cluster is C_3 for simplifying the treatment.

In the simulations performed for this study, C_3 is assumed to be the only sublimed cluster. C_3 molecules are added based on the partial pressure that is calculated at each

temperature, i.e. the number flux of C_3 molecules is calculated such that they produce the partial pressure that is expected to happen at the instantaneous particle temperature. The non-dimensional flux is calculated using Eq. 4.22 in [7] which is

$$\bar{N}_i = (n/\beta)[\exp(-s^2\cos^2\theta) + \pi^{1/2} s\cos\theta\,(1+\mathrm{erf}(s\cos\theta))]/(2\pi^{1/2}) \tag{4.1}$$

in which n is the number density in the vicinity of the surface, β is the reciprocal of the most probable molecular thermal speed, s is the molecular speed ratio which is the ration of the stream velocity to the most probable molecular thermal speed, and θ is the angle between the direction of the flux and the surface normal. In the case under consideration in this study, θ, s and β are all zero and hence equation (4.1) simplifies to

$$\bar{N}_i = n\bar{c}/4 \tag{4.2}$$

where $\bar{c}$ is the mean molecular thermal speed. Equation (4.2) reveals that the number flux of sublimed carbon clusters is only a function of the number density and mean molecular thermal speed of the sublimed carbon clusters at the vicinity of the surface. The number density is calculated based on the instantaneous partial pressure of sublimed species that is expected to happen as a result of the surface temperature. The mean thermal speed is also calculated based on the instantaneous temperature of the surface.

Since sublimed species are constantly being added to the domain at the inner boundary, the number of simulated molecules in the flow field changes during the simulation. The particle temperature at each time step is updated based on the predetermined temperature decay curves as shown in Fig. 4.1.

4.2.4 Modeling Intermolecular Collisions

The variable soft sphere (VSS) collision model [33] is used to calculate post-collision velocities of colliding molecular pairs, with the Larsen-Borgnakke model [31] to account for energy exchange between the rotational and translational modes. These two models will be discussed in the next two sections.

4.2.4.1 VSS Collision Model

In the VSS collision model, the coefficient of viscosity is assumed to have a power law dependence on temperature [7, 31]

$$\mu = \mu_{ref} \left(\frac{T}{T_{ref}} \right)^{\omega} \tag{4.3}$$

in which μ_{ref} is the viscosity at a reference temperature of T_{ref}. The VSS scattering index, ω is found by fitting Eq. (4.3) to the gas viscosity over the intended temperature range. In order to simulate the collision between molecules, the reference diameter must be known and in case of VSS model it is found from

$$d_{ref} = \left(\frac{5(\alpha+1)(\alpha+2)(m_g k_B T_{ref}/\pi)^{(1/2)}}{4\alpha(5-2\omega)(7-2\omega)\mu_{ref}} \right)^{(1/2)} \tag{4.4}$$

in which α is the exponent in the VSS model.

4.2.4.2 Larsen-Borgnakke Model

In the Larsen-Borgnakke model, the total energy of the collision pair is conserved but is redistributed between the translational and internal modes. In determining the collision dynamics for a collision pair, it should be determined first whether there is going to be inter-modal energy transfer for each or both of the molecules. The probability that each molecule undergoes energy exchange between the modes is equal to the reciprocal of the relaxation collision number [7, 9]. The collisions in which neither of the molecules undergoes inter-modal energy transfer are called elastic collisions and treated as monatomic collisions and a simple VSS scattering law is used to calculate the post collision velocities of the molecules. If at least one of the molecules is chosen for energy exchange with the internal modes, the collision is treated as inelastic, i.e. first the energy redistribution is done, then the post collision velocity of molecules is calculated using a VSS scattering model [7, 9].

Although the rotational relaxation rate is known to change with temperature, the precise nature of this relationship is unknown. Accordingly, in the present work, a constant value of 5 has been used for the rotational relaxation collision number; a parametric study has been performed to show that the simulation is relatively insensitive to variations in this parameter. The ambient gas is modeled as nitrogen, with a viscosity-temperature index of 0.74 and the reciprocal of the VSS scattering parameter of 1.36 [33].

4.2.5 Modeling C_3 Molecules

Carbon dioxide is used as a surrogate for C_3 since the structure of these two molecules is very similar (linear triatomic) and they have similar molecular weights. The number

of internal degrees of freedom for C_3 is 3.7. VSS collision parameters for $CO_2 - CO_2$, $CO_2 - N_2$ and $N_2 - N_2$ pairs are available in the literature [7] and are implemented in this study.

4.3 Results and Discussion

The purpose of the research done for this chapter has been to investigate the gas dynamics of sublimation, in particular the back flux of sublimed carbon clusters and the possible formation of shock waves. The diagrams presented in this chapter have been obtained using the previously explained transient DSMC simulation and are meant to address the two issues mentioned.

The predetermined temperature decay curves shown in Fig. 4.1 begin about 5 ns before the laser beam starts heating the particle; it also includes the laser heating period and post laser cooling period.

Fig. 4.2 is an important figure which gives some insight about the effect of fluence and particle size on sublimation phenomena. First, comparing the high fluence curves for aggregate and primary particle reveals that size of particle plays an important role in determining the significance of sublimation phenomena such as back flow. As is evident from the figure, the number flux of incident C_3 molecules on the surface of a primary particle is much smaller than an aggregate. The ratio of the maximum flux of incident C_3 molecules to the maximum sublimation flux is 1.5% for an aggregate and 0.5% for a primary particle. This shows that back flux and other sublimation phenomena are much stronger in case of an aggregate. Most of simulations from this point have been done on

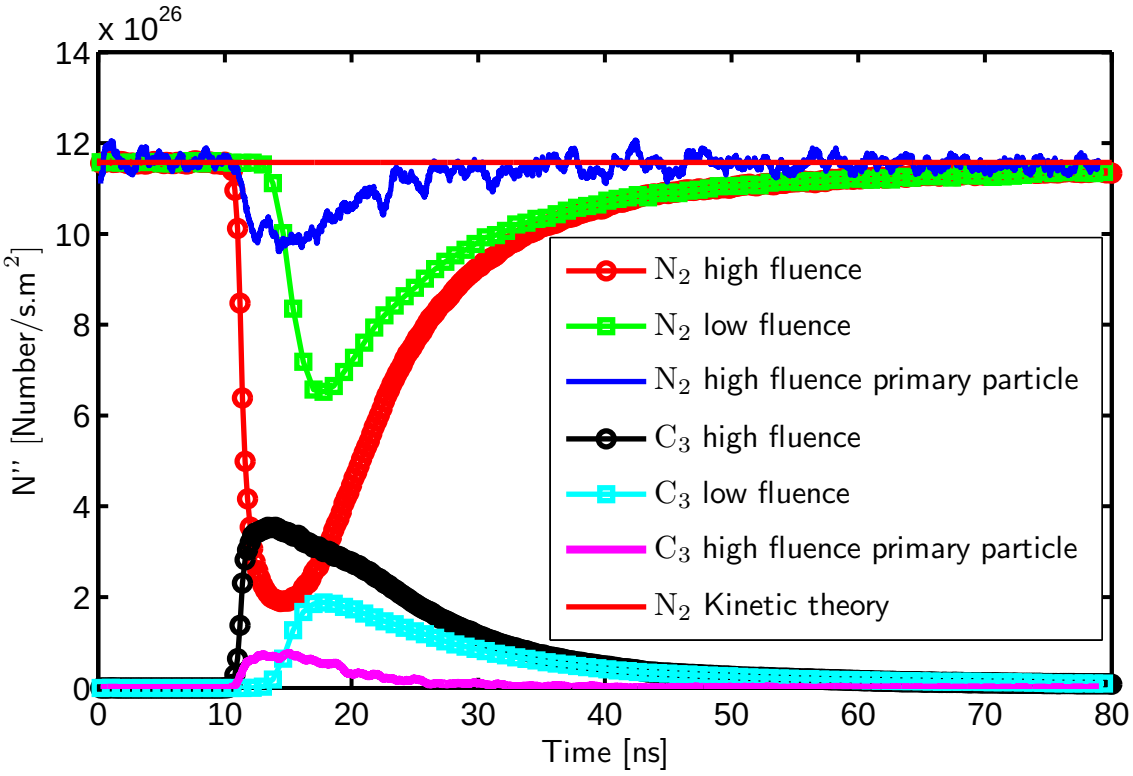

Figure 4.2: Number flux of incident molecules of N_2 and C_3 on the surface of the particle for fluences 0.436 J/cm^2 and 0.16 J/cm^2 for aggregate and for primary particle

aggregates to better show the sublimation phenomena.

Fig. 4.2 shows that, at the beginning of the laser pulse, the number flux of incident N_2 molecules decreases sharply and the number flux of incident C_3 molecules increases from zero and reaches a maximum.

When the peak of sublimation is passed, the number flux of incident C_3 molecules decreases gradually and that of N_2 molecules increases and approaches its initial value. The fact that there is a mass flux of incident C_3 molecules in Fig. 4.2 reveals a back flow of the sublimed species as a result of molecular diffusion and intermolecular collisions,

confirming some of the speculation in the literature [57]. This would greatly affect the heat transfer rate from the particles to the surrounding gas, but has been ignored in all the analytical LII sublimation models thus far. It is evident in this figure that the increase in the number flux of incident C_3 molecules and the decrease in the number flux of incident N_2 molecules are more pronounced in higher fluence compared to lower fluence which demonstrates the effect of fluence on this phenomenon. The gas dynamics of sublimation seems to be the only candidate for causing the back flux.

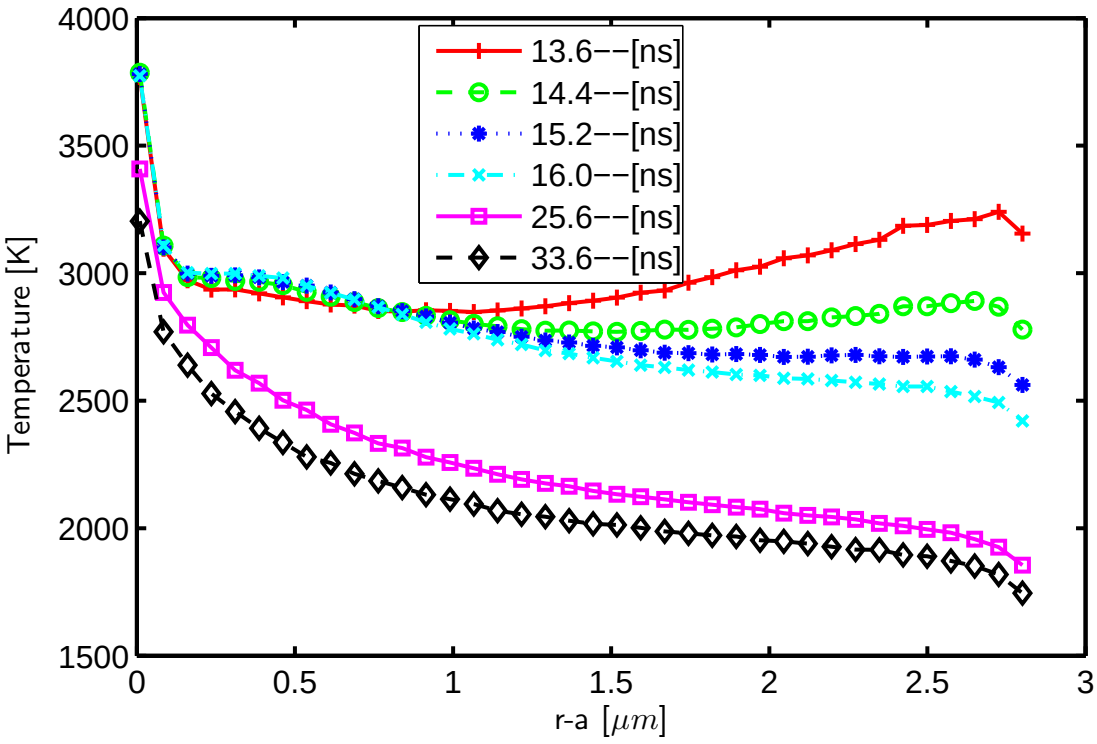

Figure 4.3: Temperature versus distance from the surface of the particle at different times for C_3 for fluence 0.436 J/cm^2

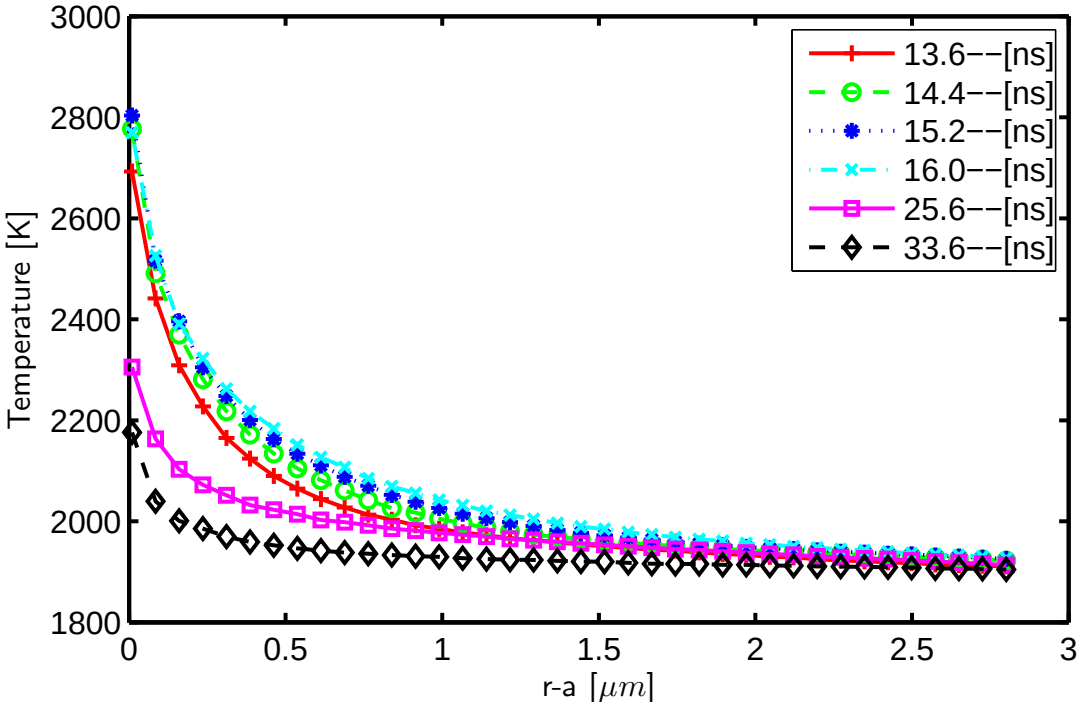

Figure 4.4: Temperature versus distance from the surface of the particle at different times for N_2 for fluence 0.436 J/cm^2

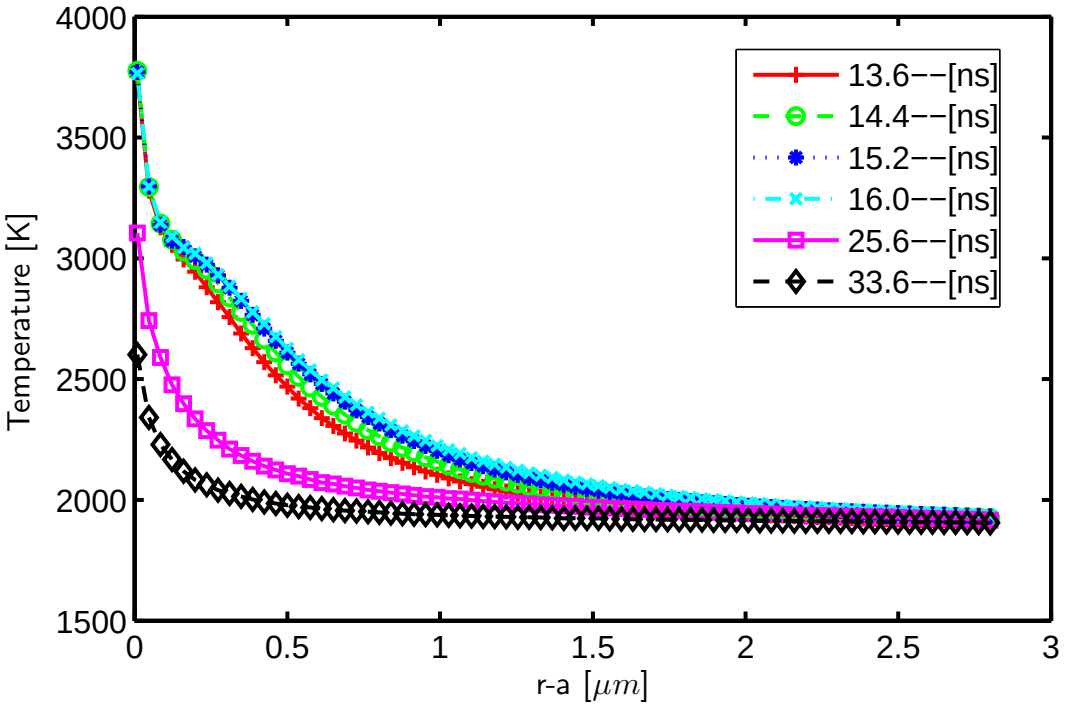

Figure 4.5: Temperature versus distance from the surface of the particle at different times for gas mixture for fluence 0.436 J/cm^2

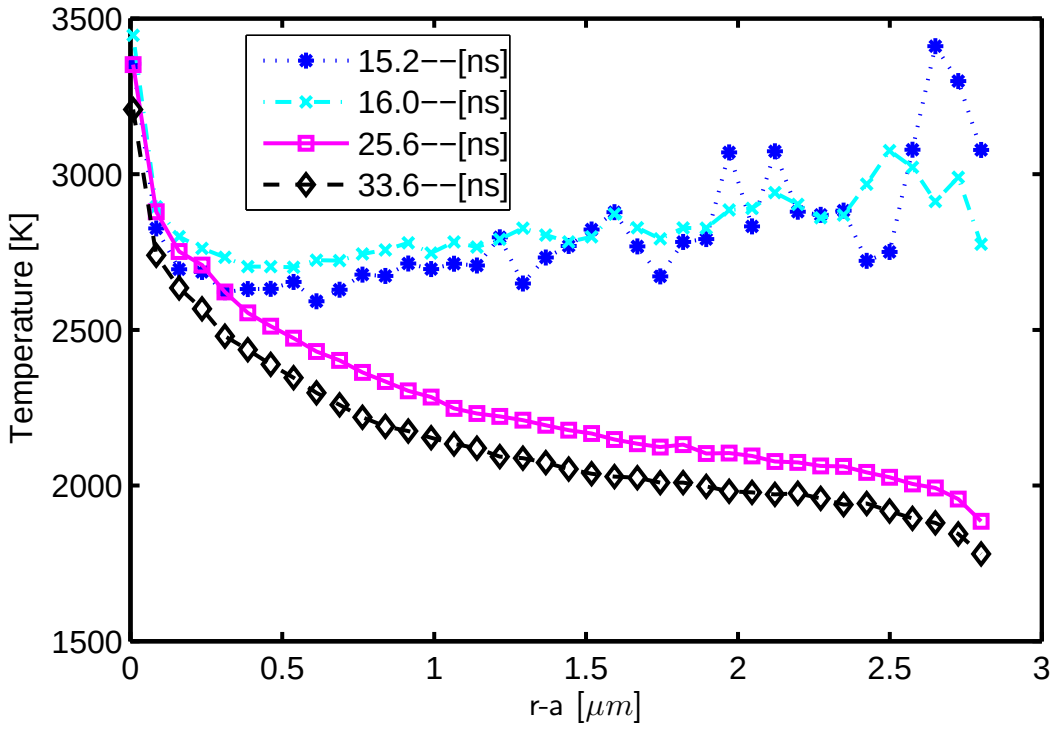

Figure 4.6: Temperature versus distance from the surface of the particle at different times for C_3 for fluence 0.16 J/cm^2

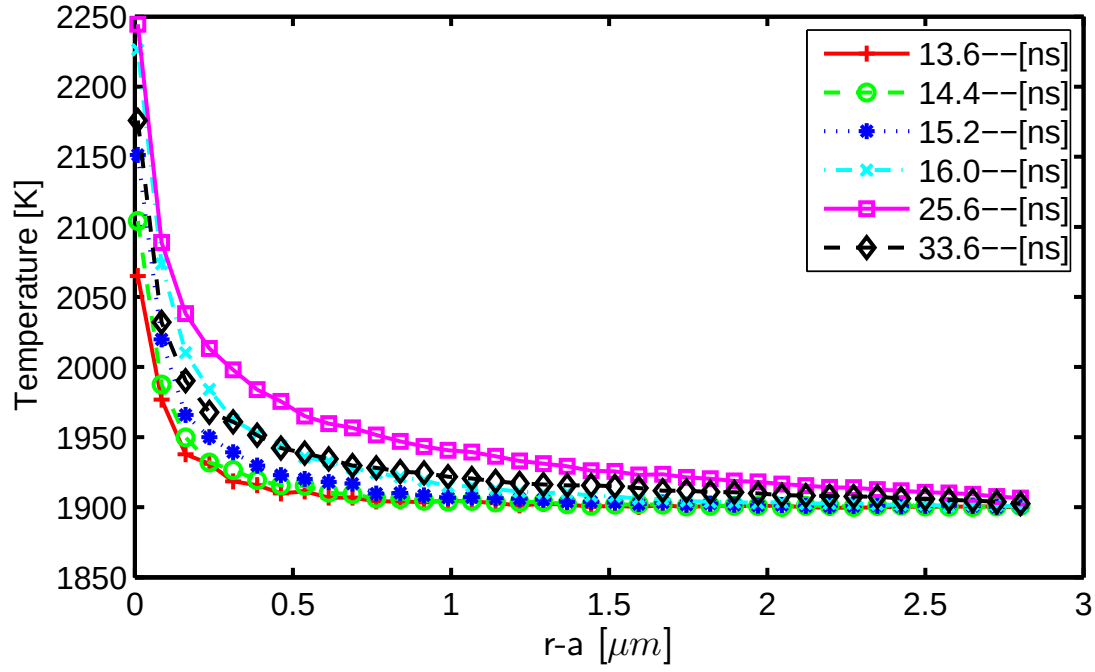

Figure 4.7: Temperature versus distance from the surface of the particle at different times for N_2 for fluence 0.16 J/cm^2

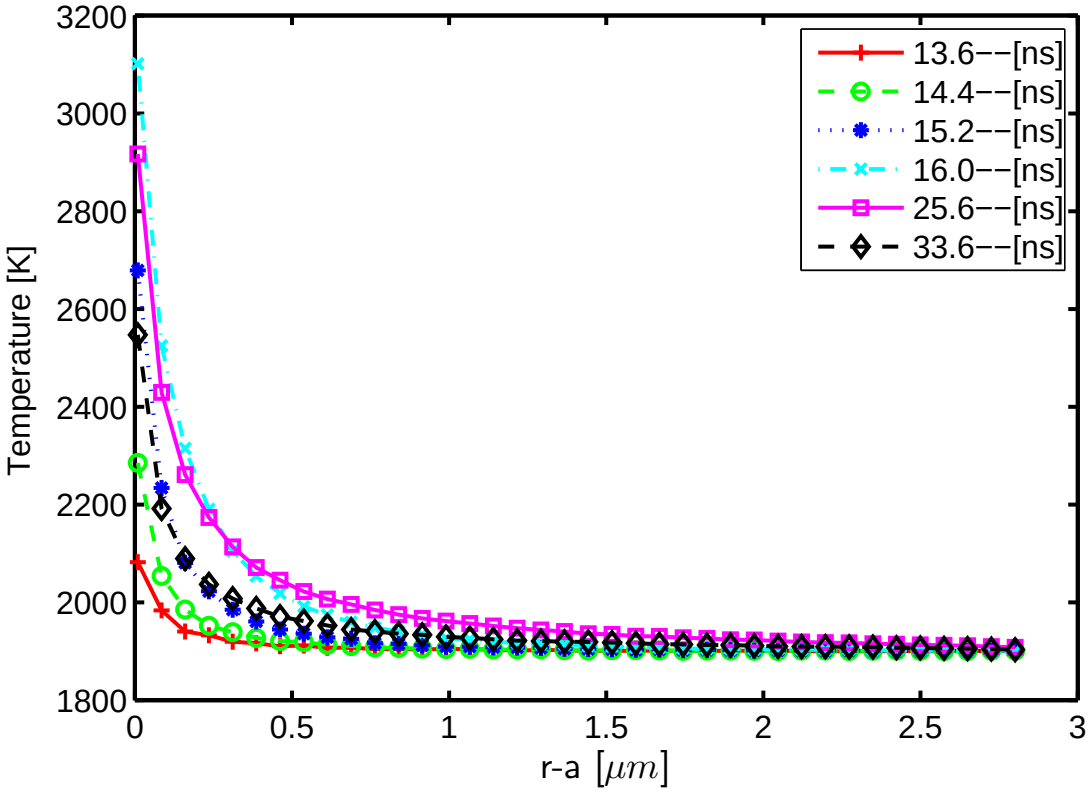

Figure 4.8: Temperature versus distance from the surface of the particle at different times for gas mixture for fluence 0.16 J/cm^2

In order to get a better understanding of the gas dynamics, it is useful to see how the temperature of the gas as a whole, as well as the temperatures of the different species, change as time passes. Fig. 4.3-Fig. 4.8, in conjunction with 4.1, illustrate how the gas responds to the temperature change of the soot particle. Fig. 4.3 shows the temperature profile of the sublimed carbon clusters, C_3, at different points in time, for a fluence of $0.436\,J/cm^2$. Carbon clusters sublime at the instantaneous temperature of the particle surface, and their mass flux is a function of the particle temperature according to Eq. (1.8), hence the average temperature of C_3 molecules near the particle surface is nearly the same as the instantaneous particle temperature. The sublimed carbon clusters also displace the N_2 molecules adjacent to the particle surface, causing the number density of N_2 to drop. When sublimation is near its peak, from 11 ns to 20 ns, C_3 molecules have a high temperature throughout the flow field. This is because there are too many C_3 molecules for the N_2 molecules to effectively quench through intermolecular collisions. When the sublimation rate begins to decline, the relative number density of C_3 molecules decreases as low temperature N_2 molecules diffuse from the outer boundary into the flow field.

Fig. 4.4 is the temperature response of initially inert N_2 gas to the same particle temperature decay curve as Fig. 4.3. As is observed from this figure, the temperature of N_2 gas increases as a result of intermolecular collisions with the C_3 molecules. Fig. 4.5 shows the temperature response of the gas mixture (both C_3 and N_2 molecules) to the same particle temperature decay curve. As expected, the gas temperature is strongly affected by the particle surface temperature when sublimation is present. The highest temperature rise is in the vicinity of the surface, where the extremely hot sublimed C_3 molecules have a

higher number density than the colder N_2 molecules. The situation is very different in low fluence LII when there is no sublimation, and correspondingly there will be a significant temperature jump near the particle surface as will be seen later.

Figs. 4.6, 4.7 and 4.8 are counterparts of Figs. 4.3, 4.4, 4.5 for a lower fluence of $0.16\,\mathrm{J/cm^2}$. The effect of lower sublimation rate on temperature profile of C_3, N_2 and that of the gas mixture as a whole is that temperature is lower at any point and at any time.

Fig. 4.9 and Fig. 4.10 show the number density profile of C_3 molecules at different times for fluence of $0.436\,\mathrm{J/cm^2}$. Fig. 4.9 shows that the number density of C_3 molecules increases with time until the particle temperature reaches its peak. Fig. 4.10 on the other hand shows the gradual decline in the number density of C_3 molecules throughout the domain as the particle temperature decreases. The shape of the curves in these two plots also reveals that there is no shock wave; instead, C_3 molecules propagate mainly by diffusion. If there were a shock wave, one would observe a sudden increase in number density that would propagate away from the surface like a wave. The pressure profiles, as shown in Figs. 4.11 and 4.12, also reveal no shock wave.

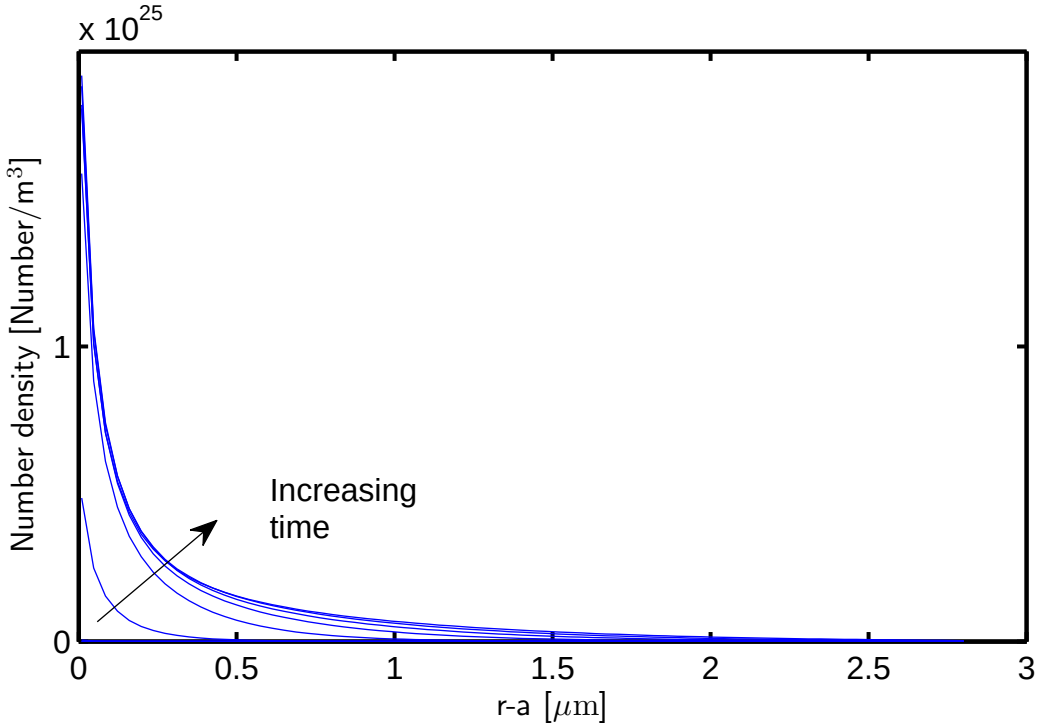

Figure 4.9: Number density versus distance from the surface of the particle at 11 different times from 6.4 ns to 14.4 ns with equal increments for C_3 for fluence 0.436 J/cm^2

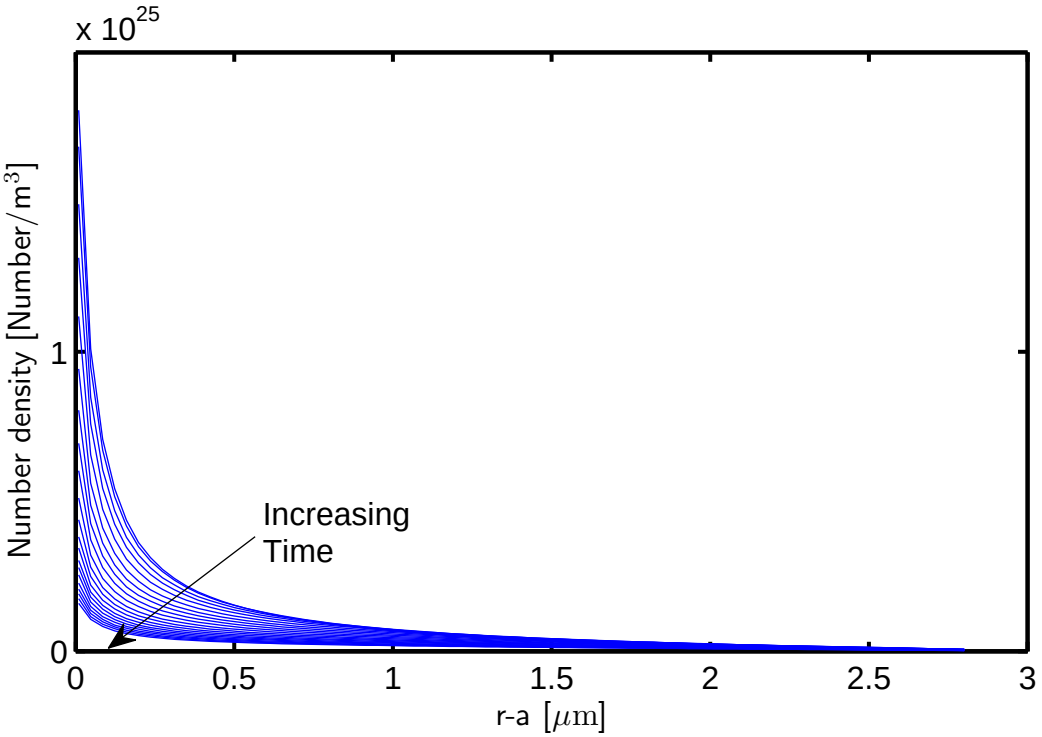

Figure 4.10: Number density versus distance from the surface of the particle at 21 different times from 14.4 ns to 30.4 ns with equal increments for C_3 for fluence 0.436 J/cm^2

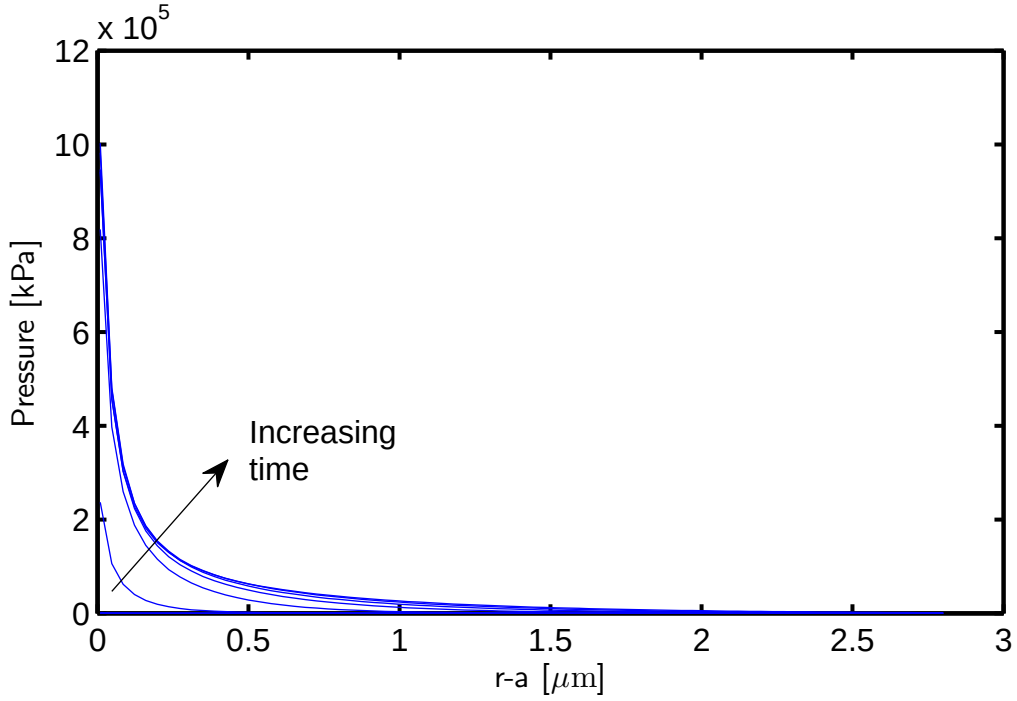

Figure 4.11: Pressure versus distance from the surface of the particle at 11 different times from 6.4 ns to 14.4 ns with equal increments for C_3 for fluence 0.436 J/cm^2

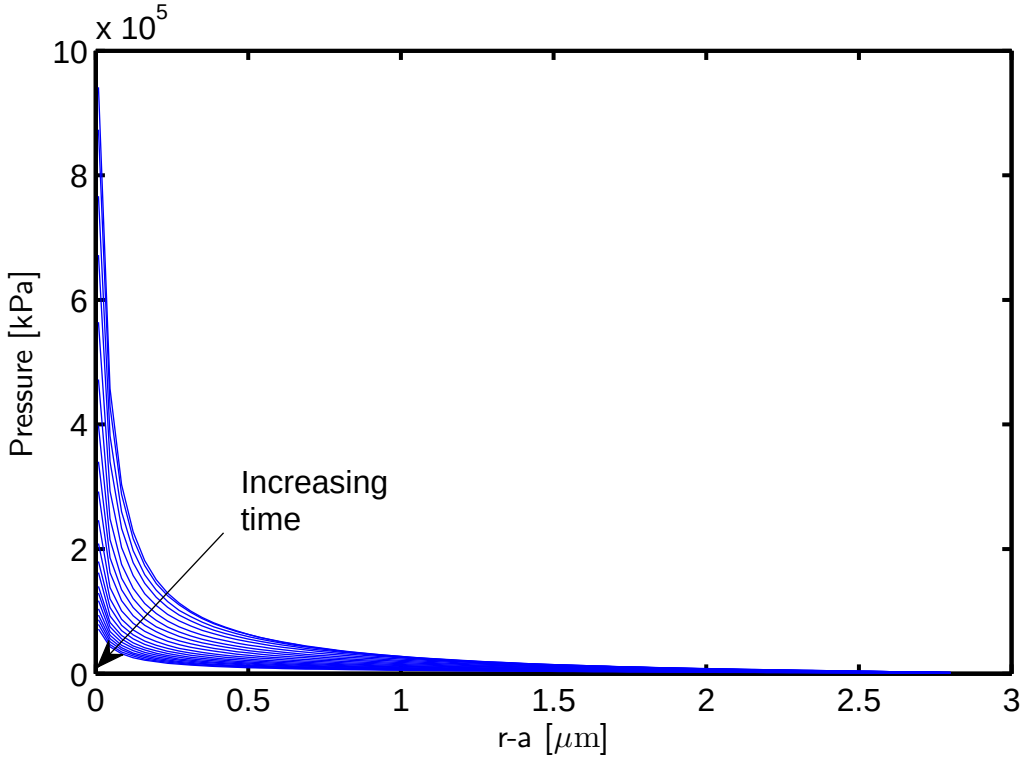

Figure 4.12: Pressure versus distance from the surface of the particle at 11 different times from 14.4 ns to 30.4 ns with equal increments for C_3 for fluence 0.436 J/cm^2

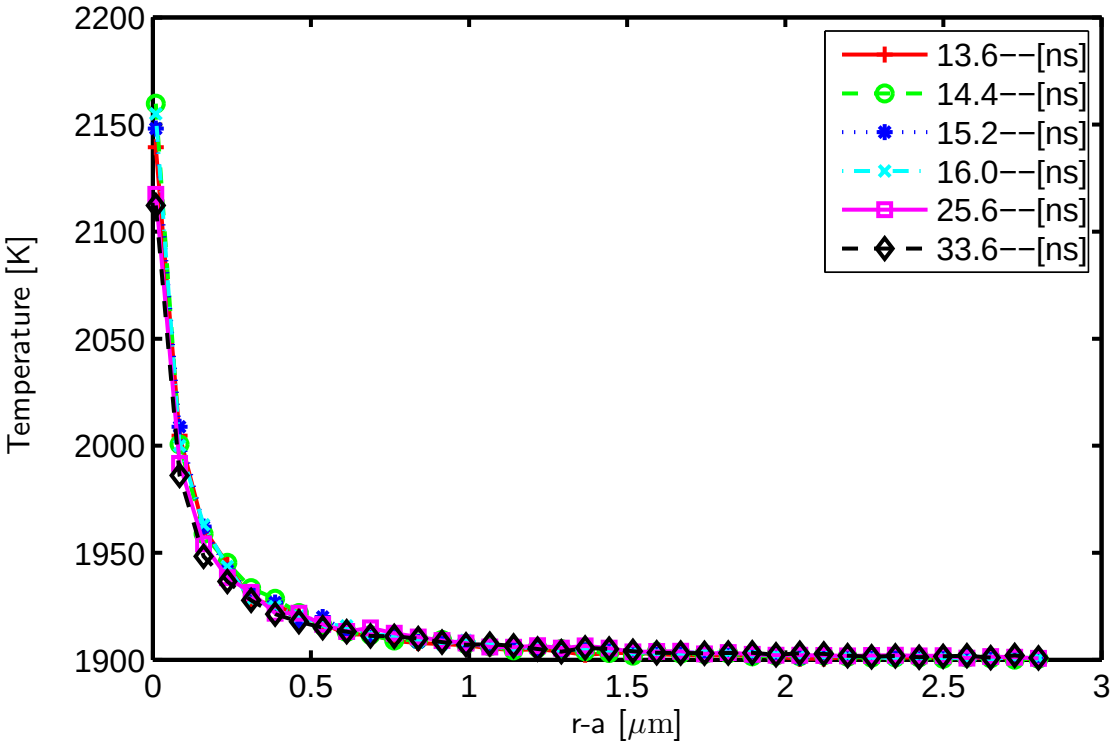

Figure 4.13: Temperature versus distance from the surface of the particle at different times for gas mixture for fluence 0.436 J/cm^2 for a case without sublimation

To highlight how the sublimed species influence gas dynamics, an additional simulation has been run in which the particle temperature for a fluence of 0.436 J/cm^2 is used, but sublimation has been excluded from the model. Fig. 4.13 shows that without sublimation, the gas temperature near the surface increases much less than when sublimation is happening, resulting in a much larger temperature jump between the gas temperature and the particle temperature. This difference is due to the fact that, when sublimation is occurring, the extremely hot sublimed carbon clusters heat the N_2 molecules near the particle surface through intermolecular collisions but this mechanism is absent when there is no sublimation.

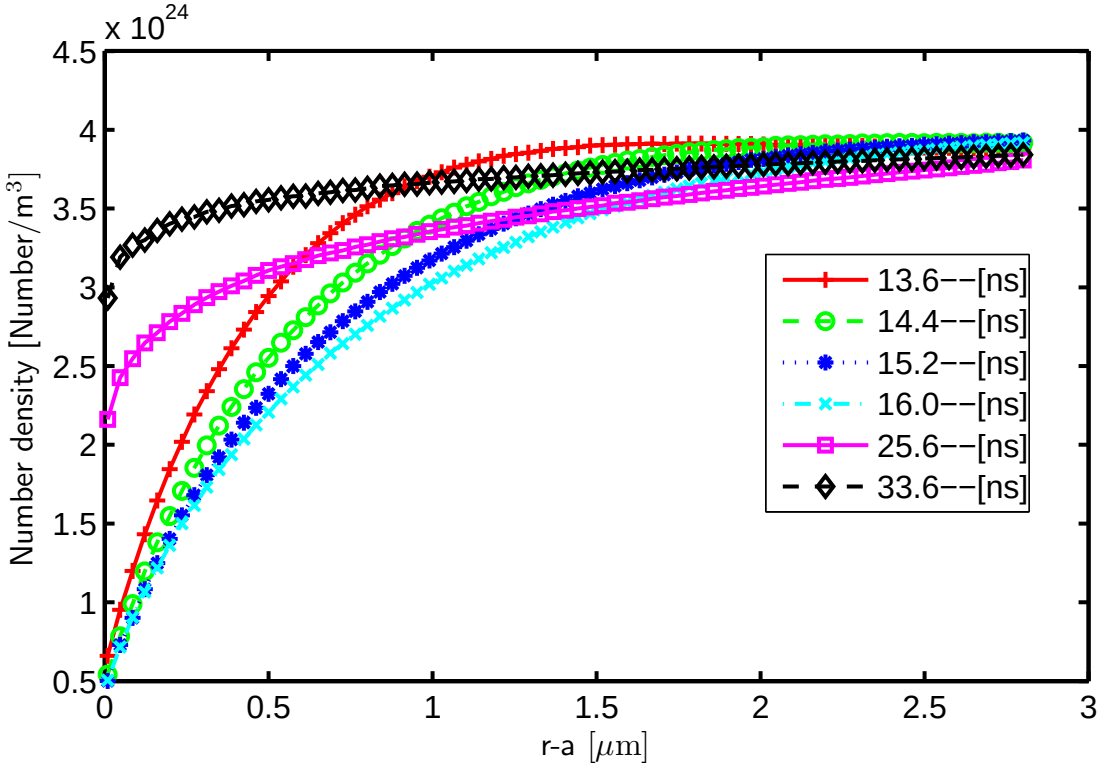

Figure 4.14: Number density versus distance from the surface of the particle at different times for gas mixture for fluence 0.436 J/cm^2

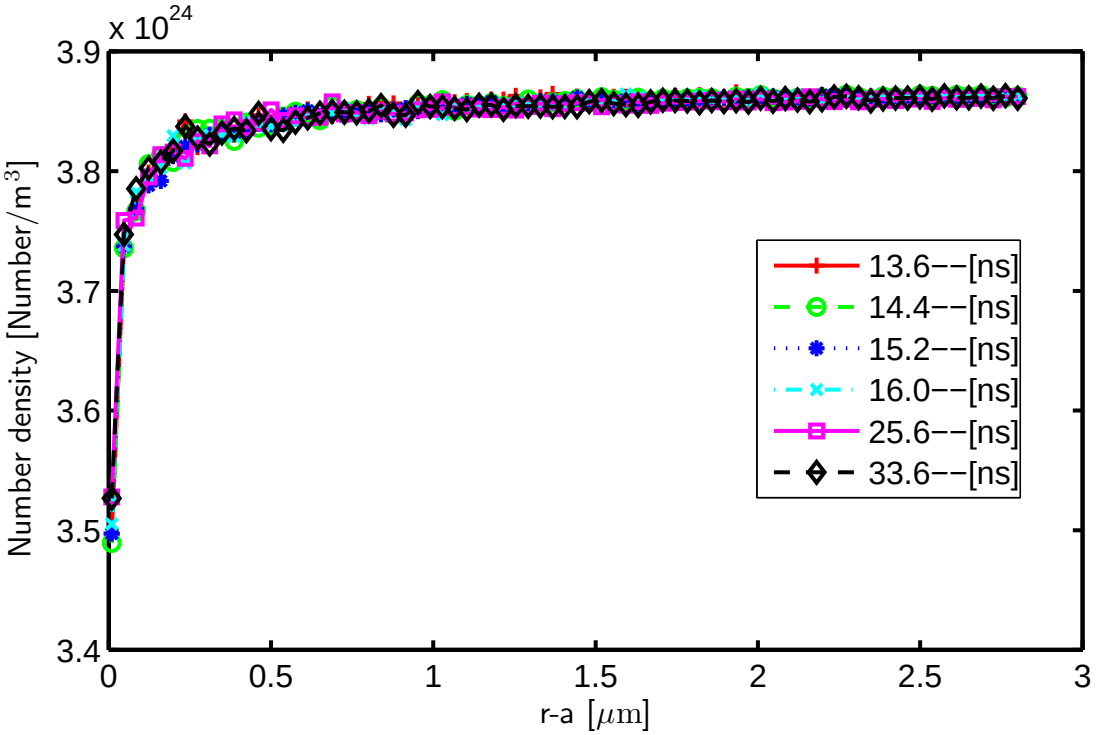

Figure 4.15: Number density versus distance from the surface of the particle at different times for gas mixture for fluence 0.436 J/cm^2 for a case without sublimation

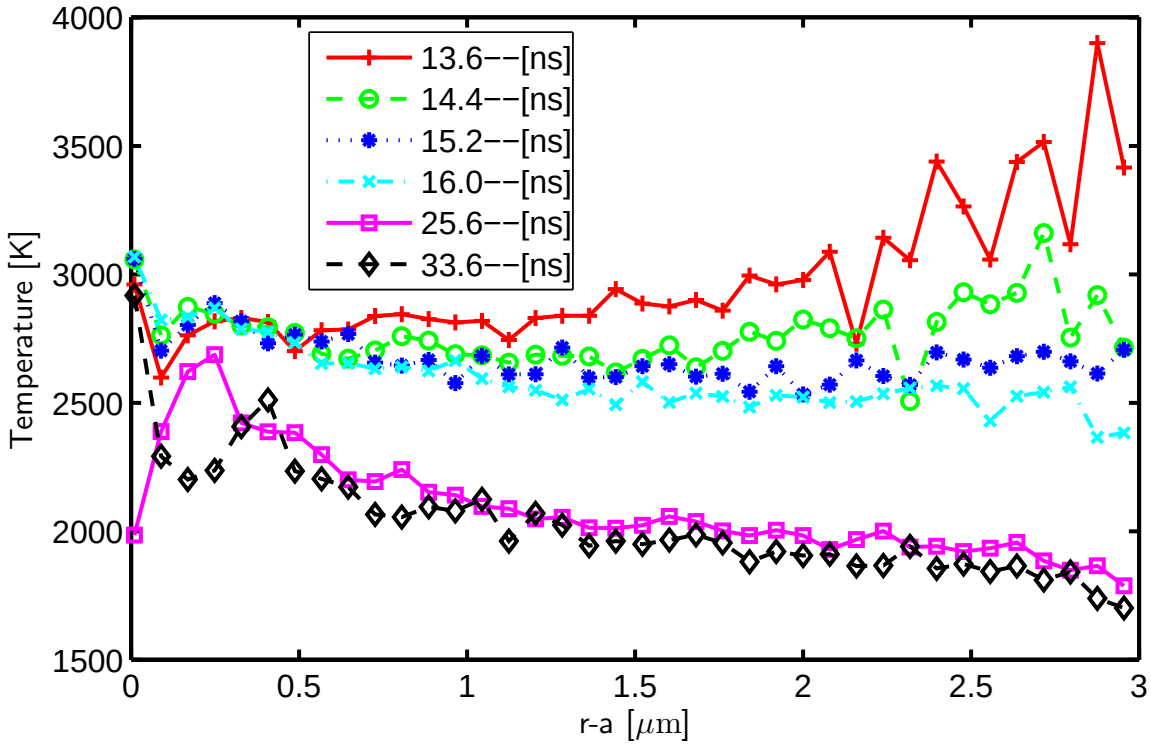

Figure 4.16: Temperature versus distance from the surface of the particle at different times for C_3 for fluence 0.436 J/cm^2 for a Primary particle

Fig. 4.14 and Fig. 4.15 give some additional insight about the gas dynamics of sublimation. The simulation that yielded Fig. 4.15 is exactly similar to that of Fig. 4.14, but again, it excludes sublimation physics. Fig. 4.14 shows a much more significant density decrease for N_2 compared to Fig. 4.15. This is due to the sudden expansion of the sublimed species, which displace the nitrogen molecules and decrease their concentration near the surface. As noted above, this phenomenon would have a significant effect in reducing the rate of conduction heat transfer in the corresponding period.

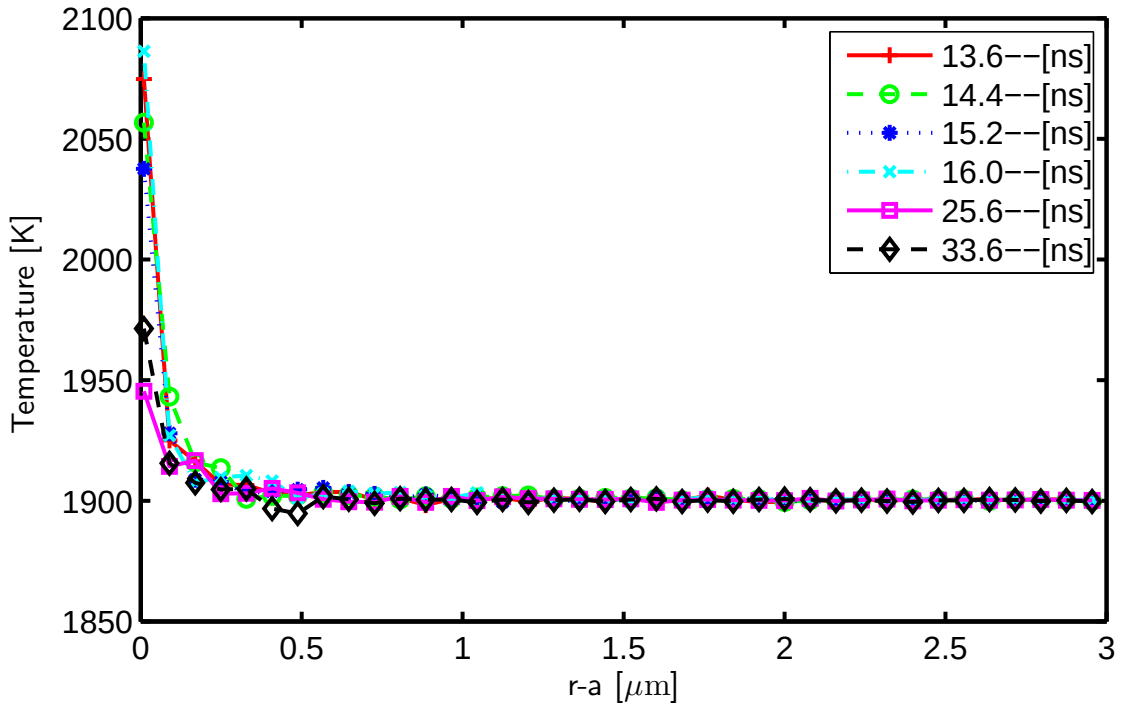

Figure 4.17: Temperature versus distance from the surface of the particle at different times for N_2 for fluence 0.436 J/cm^2 for a Primary particle

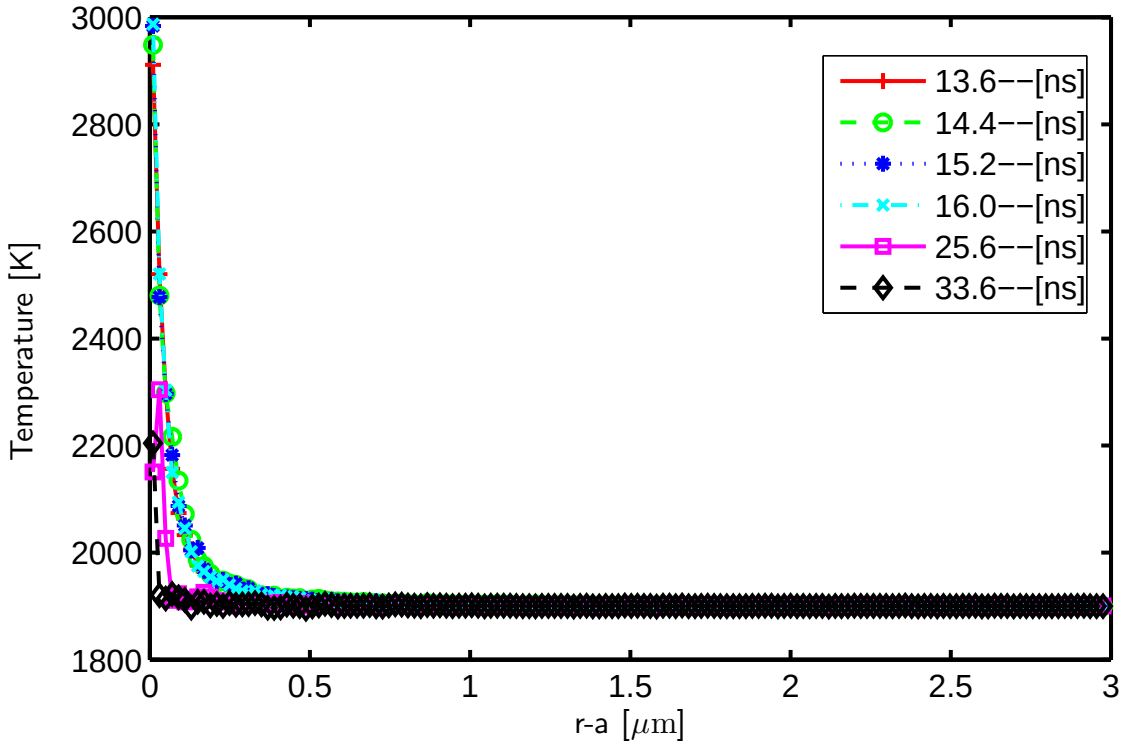

Figure 4.18: Temperature versus distance from the surface of the particle at different times for gas mixture for fluence 0.436 J/cm^2 for a Primary particle

As mentioned before, the back flux of sublimed clusters is much smaller in case of primary soot particle. Still it is illustrative to compare temperature, number density and other plots of a primary particle with their counterparts for soot aggregate. Comparing Fig. 4.16 and Fig. 4.3, reveals that the size of the subliming body does not significantly influence the temperature of C_3 molecules in the domain, especially far from the particle. In fact, the temperature of the C_3 molecules right after they sublime from the surface is the same in both cases and the percentage of C_3 molecules that undergo collisions with N_2 molecules will also be nearly the same far from the surface where the density of N_2 is similar in both cases, this is why the temperature of C_3 is approximately the same far from the surface in both cases. But the number of hot C_3 molecules is larger in case of an aggregate and they can affect the temperature of N_2 molecules more as Fig. 4.4 and Fig. 4.17 show and hence the temperature of the gas mixture as a whole will be higher as is perceptible from comparing Fig. 4.18 and Fig. 4.5. Fig. 4.19 is the result of two theoretical simulations in which the temperature of the particle is kept constant at 5000 K to yield a significant rate of sublimation.

Finally we consider the case where the domain is initially a vacuum and no N_2 molecule enters the system from the outer boundary, in the other case, the domain is full of N_2 molecules at atmospheric pressure and the pressure of the outer boundary is kept constant. Even in case of vacuum, there still exists a strong back flux of C_3 molecules on the surface which is comparable to the other case. This reveals that the back flux is mainly due to collision between C_3 molecules near the surface. It was shown before that as sublimation continues, the N_2 molecules are driven away from the neighborhood of the surface, but in Fig. 4.19, in case of atmospheric pressure, the rate of back flux reaches a constant value

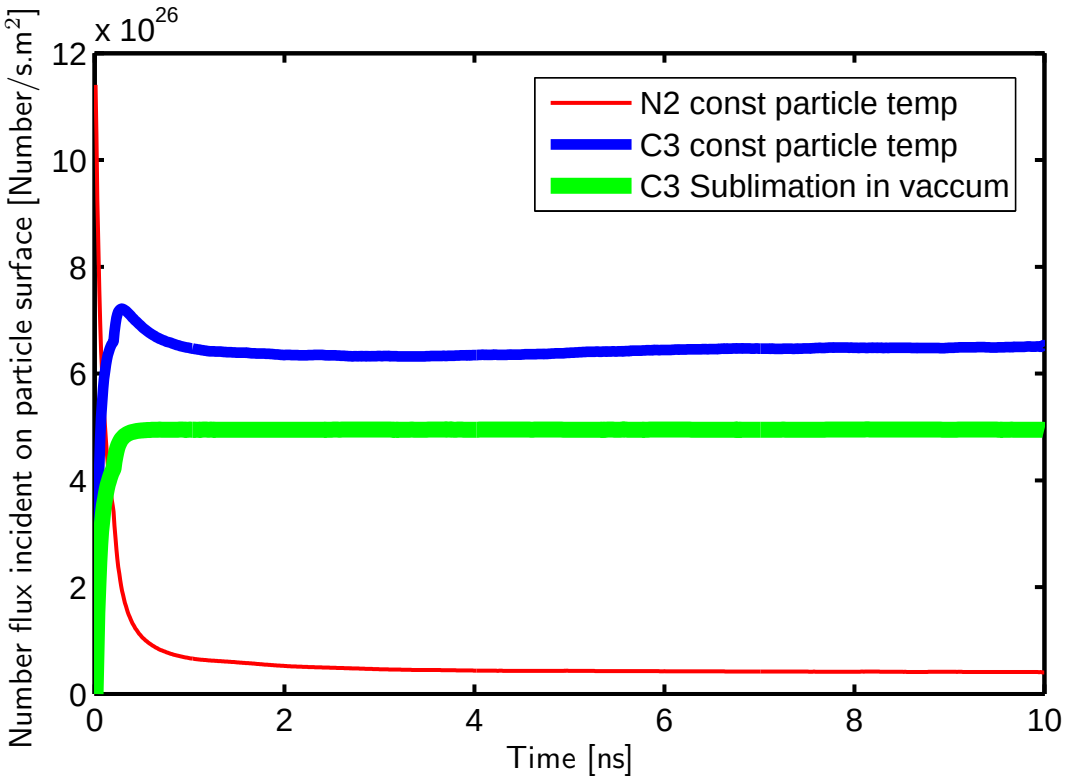

Figure 4.19: Number flux of incident molecules of N_2 and C_3 on the surface of the particle for constant particle temperature of 5000 K for an aggregate

and does not change as time passes, this shows that after the N_2 molecules are driven away, it is the collision between C_3 molecules that continues to cause the back flux.

In order to get a better understanding about the gas dynamics of back flux of C_3 molecules, the velocity of molecules that are sublimed from the surface at a certain time, as well as those which are reflected from the surface or are incident on the surface have been sampled for a theoretical case with constant particle temperature of 5000 K as is shown in Fig. 4.20. The duration of the sampling is from 2 ns up to 2 ns + one time step. At each run, at any time range, some C_3 molecules are incident on and some are reflected

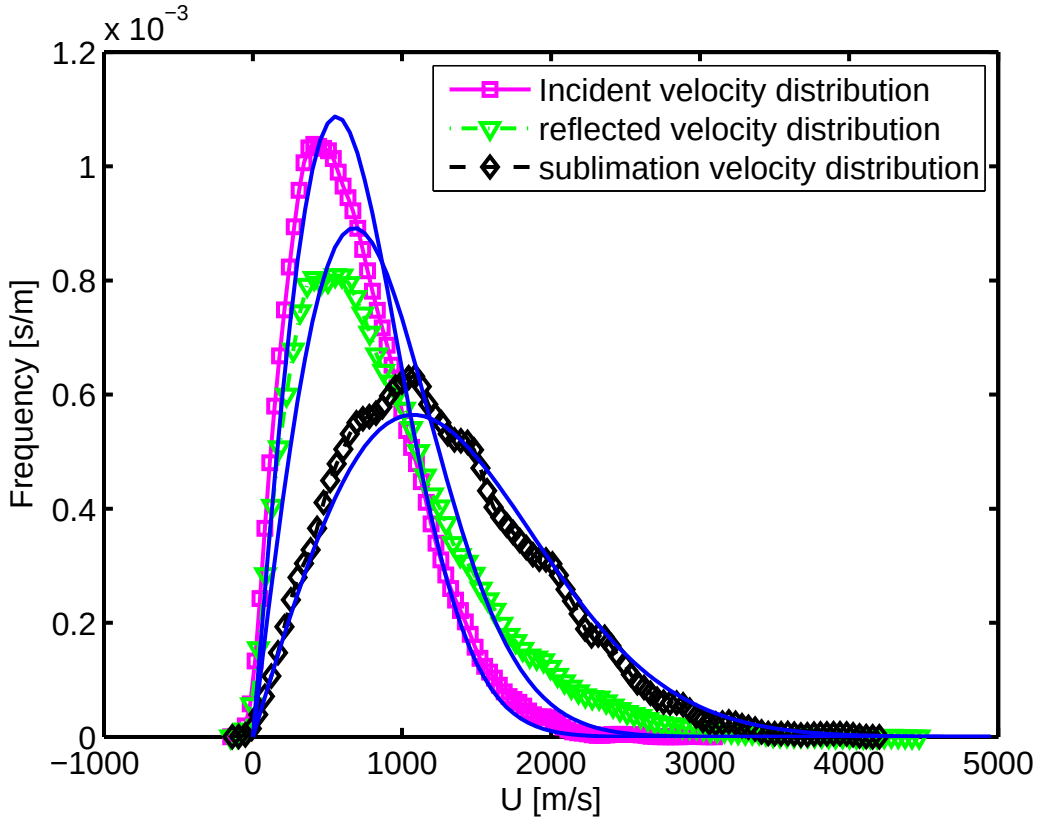

Figure 4.20: velocity distribution of subliming, reflected and incident C_3 molecules from the surface for constant particle temperature of 5000 K at 2 ns from the beginning of simulation

or sublimed from the surface; the codes have been modified such that they can store the velocity of all of these molecules at any pre-specified time period.

Molecules are sublimed at surface temperature; this is why the Maxwellian curve at surface temperature is such a good fit on the sublimation curve. For the other two velocity distributions, an equivalent Maxwellian temperature has been found by using the least squares regression. The corresponding Maxwellian temperature of the incident velocity distribution and reflected velocity distribution has been found to be 1347 K and 2002 K

respectively. Two Maxwellian curves have been drawn with these temperatures as shown on the figure and they are in a very good agreement with the distribution of the sampled velocities. The fact that the characteristic temperature of the incident C_3 molecules is much smaller than that of the subliming molecules shows that most of these molecules have undergone collisions at a distance from the surface which is roughly the outer edge of the Knudsen layer. The heat transfer in this case happens in the transition regime and there is a collisionless Knudsen layer in the vicinity of the surface. The reason why the characteristic temperature of the reflected molecules in higher than incident molecules is that the accommodation coefficient is 0.35 which means some of the collisions are diffuse collisions and hence their reflected velocities have the characteristic temperature of the surface which is higher than the characteristic temperature of the incident molecules.

4.4 Conclusion

This chapter presents the first transient DSMC investigation of the gas dynamics associated with high fluence TiRe-LII. Particle temperatures are taken from modeled temperature decay curves reported in the literature. Intermolecular collisions are simulated with the Larsen-Borgnakke model, using the collision parameters of CO_2 as a surrogate for C_3.

The simulations in this study show that during sublimation, some of the sublimed clusters will return back to the surface of the subliming particle as a result of intermolecular collisions with the inert gas and with each other. This also results in a considerably higher gas temperature close to the surface, compared to simulations in which the sublimation submodel is deactivated. This effect has been excluded in analytical sublimation mod-

els used by TiRe-LII practitioners to date. Our simulations also show that, contrary to speculation in the literature, shock waves do not appear to form under the high fluence conditions explored in this study. In fact even in the extreme theoretical case of constant particle temperature of 5000 K which is suddenly applied to the particle (as a step function) no shock wave was observed.

Chapter 5

Conclusions and Future Work

5.1 Transient Transition Regime Heat Conduction in LII

Heat transfer can happen in one of the three regimes, namely, free molecular, continuum, and transient. Analytical solutions have been developed for the governing Boltzmann equation for the two limiting cases of continuum and free molecular, but not for transition regime which is analytically intractable. Generally there are four approaches to model heat transfer in transition regime; approximate analytical technique, Interpolation technique, two layer technique, and numerical approach.

In the research performed for chapter 3, transient DSMC simulation is the numerical tool that is used for modeling transient transition regime conduction.

There are some still unresolved phenomena in LII. "anomalous cooling" for instance is

an effect which remains unexplained to date; it is the very high initial rate of cooling that cannot be predicted by ordinary LII models. The duration of this effect is $\sim$ 50ns after the peak of the laser pulse and there has been some speculation about the causes but none have been proved yet. Among the possible causes are, evaporation of desorbed volatiles at temperatures less than sublimation threshold of carbon, or the speculated detachment of hydrogen and oxygen atoms from the surface of soot which causes conversion of carbon atoms from sp^3 to sp^2 hybridization states. Another cause which has been proposed by the performers of this research is the transient conduction effects. All the LII models operate based on steady state assumption and none considers the transient effects.

In this study transient DSMC simulations have been used to determine the significance of transient effects in chapter 3. The heat transfer predicted by transient DSMC and steady state DSMC have been compared which highlights the finite response time of gas. This finite response time causes an increased heat transfer rate in the transient DSMC compared to steady state DSMC. In fact the increase gas temperature causes a thermal expansion which drives molecules away from the surface of the particle and reduces the density of gas near the surface leading to reduced heat transfer rate. Accordingly at longer times at any surface temperature the density of gas near the surface is smaller for the steady state DSMC compared to transient DSMC, this difference is significant for the first 50 ns where the gas is unable to respond fast enough to the sudden increase in particle temperature, but after that, transient effects lose their significance and the gas will be able to respond fast enough to the more gradual changes in particle temperature.

Based on the simulation results, the amount of enhanced cooling that can be solely attributed to transient gas dynamics effects is smaller than the amount of anomalous

cooling observed from sensible energy loss calculations, but the duration of both effects are similar ($\sim$ 50 ns).

A scale analysis was done by Filippov and Rosner [15] in 2000 to determine the importance of transient effects. In this scale analysis the characteristic time of particle cooling has been compared to the characteristic equilibration time of gas. Based on this approach, it is predicted that transient effects are not important and the steady state treatment which has been used in LII is exact.

The author believes that this scale analysis has some inherent weaknesses. The most significant weakness in Filippov and Rosner analysis [**?**] is that they are trying to estimate the characteristic equilibrium time of gas while there is no equilibrium in LII. Equilibrium conditions are valid only when there are no temporal or spatial gradients while both exist in LII. Another approach for calculating the time scale based on using a more physical length scale has been offered in this thesis which estimates the time it takes for gas to reach steady state rather than equilibrium or quasi-equilibrium. This time scale has been found based on a continuum analysis which is just an estimation of the physics of LII and is consistent with DSMC results. It is still possible to define a more physical characteristic time. More research needs to be done to find the more significant causes of anomalous cooling.

5.2 Sublimation in High Fluence LII

The importance of sublimation in LII depends mainly on laser pulse fluence. When fluence is high enough to cause sublimation, the LII experiment is called high fluence LII. Sublima-

tion in LII is a thermal process, i.e. the drive for sublimation is the increase in temperature of the soot particles above the sublimation threshold. There are various sources of uncertainty in the sublimation mechanism including annealing of the surface of soot, oxidation, and gas dynamics of sublimed species.

The focus of chapter 4 in this thesis is investigation of gas dynamics of sublimation. In particular two effects have been considered; back flux of sublimed species and supersonic expansion of sublimed clusters or in other terms, formation of shock waves.

For simplicity, C_3 is considered to be the only subliming species which is an assumption done in most of LII models. Moreover N_2 has been used to model air. Transient DSMC code has been modified to produce a jet of sublimed clusters at instantaneous surface temperature with a Maxwellian velocity distribution.

The results verify that some of the sublimed species will return back on the surface of the particle as a result of intermolecular collisions with each other and with inert N_2 molecules. The interesting finding is that the main cause of back flux is the inter-collision between sublimed clusters, whereas N_2 molecules are unimportant in driving the back flux.

The number density and pressure profiles obtained for the predetermined temperature curves in the DSMC simulations reveal no supersonic expansion of sublimed clusters. Other than the predetermined temperature curves, some theoretical cases have been run with suddenly applied very high constant particle temperature, but still no shock wave is observed.

5.3 Future Work

In this section some of the possible paths for future research and some modifications that could improve the results are discussed.

5.3.1 Possible Modifications and Improvements

One possible alternative to the simulation done in chapter 3 is to model real combustion situation where all combustion products are present instead of using argon as the surrounding gas.

There can also be an improvement in the scale analysis done to determine the importance of transient effects in LII. A still more physical characteristic time for the response time of the gas to transient effects could be defined.

Moreover, sublimation models could be made more sophisticated if the sublimation of all the carbon clusters is considered instead of using only C_3. Moreover, an important improvement to the simulations could be done if the change in the temperature of the outer boundary could be taken account for. This would increase the accuracy of the results especially at long times. The effect of pressure, particle size and other parameters on sublimation can also be investigated.

Modeled predetermined temperature decay curves have been used in chapter 4 due to unavailability of experimentally measured temperature response of the particles during the laser pulse; if such curves become available in the future, they could be used instead in the simulations. Nonetheless, using those curves will not change the qualitative conclusions

reached in this thesis.

5.3.2 Problems that could be investigated

An important contribution could be made using a sufficiently sophisticated transient DSMC code to model the change in particle temperature based on the instantaneous heat transfer rate from the particle instead of using a predetermined temperature decay curve. This could be done both in case of low fluence LII where conduction dominates and high fluence LII where there is sublimation.

Another important problem that could be investigated in future is the problem of gas heating in the laser beam area. This problem was first proposed by Snelling et al, [57] where they observed the area heated by laser pulse gets heated and the temperature of gas increases and cannot relax back to ambient temperature in the time between two successive pulses. A continuum based numerical simulation is planned to be done to investigate this issue by assuming that each suspended nano-particle is a point heat source.

The non-thermal photo ablation of desorbed species could also be investigated using a sophisticated version of DSMC code. There are various sources of uncertainty about the structure of soot and it is not known very well how much of the surface of soot particle is covered by PAHs, but more research could be done regarding this issue which is one of the most important sources of uncertainty in LII models.

In literature, some researchers [12] have tried to estimate the accommodation coefficient for soot particles at low fluence where there is no sublimation. In future, the accommodation coefficient of soot at high fluence will be investigated by using a hybrid combination

of molecular dynamics (MD) method and DSMC.

Another research that could be done using transient DSMC is to predict heat transfer due to sublimation and investigate the effect of back flux of sublimed clusters on heat transfer. The effect of reattachment of the incident carbon species can be evaluated using transient DSMC simulations.

Another computationally demanding simulation which is worthwhile is to model sublimation from a 3D aggregate instead of modeling the aggregate as an sphere.

References

[1] RL Armstrong and A Zardecki. Diffusive and convective vaporization of irradiated droplets. *Journal of applied physics*, 62(11):4571–4578, 1987.

[2] International Carbon Black Association et al. Carbon black user's guide, safety, health, & environmental information. *International Carbon Black Association*, 2004.

[3] Thomas R Barfknecht. Toxicology of soot. *Progress in energy and combustion science*, 9(3):199–237, 1983.

[4] Timothy G Benish, Arthur L Lafeur, Koli Taghiadeh, and Jack B Howard. c_2h_2 and pah as soot growth reactants in premixed c_2h_4-air flames. In *Symposium (International) on Combustion*, volume 26, pages 2319–2326. Elsevier, 1996.

[5] Mario Bertero and Patrizia Boccacci. *Introduction to inverse problems in imaging*. Taylor & Francis, 2010.

[6] Prabhu Lal Bhatnagar, Eugene P Gross, and Max Krook. A model for collision processes in gases. i. small amplitude processes in charged and neutral one-component systems. *Physical review*, 94(3):511, 1954.

[7] GA Bird. Molecular gas dynamics and the direct simulation of gas flows, clarendon press, oxford, 1994.

[8] Henrik Bladh and P-E Bengtsson. Characteristics of laser-induced incandescence from soot in studies of a time-dependent heat-and mass-transfer model. *Applied Physics B*, 78(2):241–248, 2004.

[9] Claus Borgnakke and Poul S Larsen. Statistical collision model for monte carlo simulation of polyatomic gas mixture. *Journal of computational Physics*, 18(4):405–420, 1975.

[10] David William Burr. Inverse analysis of light scattered by soot aggregates. 2010.

[11] C Cercignani and CD Pagani. Variational approach to rarefied flows in cylindrical and spherical geometry. In *Rarefied Gas Dynamics, Volume 1*, volume 1, page 555, 1967.

[12] KJ Daun, GJ Smallwood, and F Liu. Investigation of thermal accommodation coefficients in time-resolved laser-induced incandescence. *Journal of heat transfer*, 130(12), 2008.

[13] KJ Daun, Gregory J Smallwood, and Fengshan Liu. Molecular dynamics simulations of translational thermal accommodation coefficients for time-resolved lii. *Applied Physics B*, 94(1):39–49, 2009.

[14] Virendra K Dogra, James N Moss, Richard G Wilmoth, and Joseph M Price. Hypersonic rarefied flow past spheres including wake structure. *Journal of Spacecraft and Rockets*, 31(5):713–718, 1994.

[15] AV Filippov and DE Rosner. Energy transfer between an aerosol particle and gas at high temperature ratios in the knudsen transition regime. *International journal of heat and mass transfer*, 43(1):127–138, 2000.

[16] AV Filippov, My Zurita, and DE Rosner. Fractal-like aggregates: relation between morphology and physical properties. *Journal of Colloid and Interface Science*, 229(1):261–273, 2000.

[17] Michael Frenklach. Reaction mechanism of soot formation in flames. *Physical Chemistry Chemical Physics*, 4(11):2028–2037, 2002.

[18] NA Fuchs. Uber die verdampfungsgeschwindigkeit kleiner tropfchen in einer gasatmosphare. *Physikalische Zeitschrift der Sowjetunion6*, pages 224–243, 1934.

[19] Nikolaj A Fuks and Aleksandr Georgievich Sutugin. *Highly dispersed aerosols*. Ann Arbor Science Publishers, 1970.

[20] James Hansen and Larissa Nazarenko. Soot climate forcing via snow and ice albedos. *Proceedings of the National Academy of Sciences of the United States of America*, 101(2):423–428, 2004.

[21] Per Christian Hansen. *Rank-deficient and discrete ill-posed problems: numerical aspects of linear inversion*, volume 4. Society for Industrial and Applied Mathematics, 1987.

[22] J Johnsson, H Bladh, N-E Olofsson, and P-E Bengtsson. Influence of soot aggregate structure on particle sizing using laser-induced incandescence: importance of bridging between primary particles. *Applied Physics B*, pages 1–12, 2012.

[23] Andrei Kazakov and Michael Frenklach. On the relative contribution of acetylene and aromatics to soot particle surface growth. *Combustion and flame*, 112(1):270–274, 1998.

[24] Earle H Kennard and Earle H Kennard. *Kinetic theory of gases: with an introduction to statistical mechanics*. McGraw-hill New York, 1938.

[25] W Ketren, P Vallikul, A Garo, and G Grehan. Numerical simulation on effects of laser fluence on temporal and time integrated lii-process of soot particle. *Journal of Sustainable Energy & Environment*, 1:173–179, 2010.

[26] Nino Kunzli, Reinhard Kaiser, Sylvia Medina, M Studnicka, Olivier Chanel, Paul Filliger, Max Herry, F Horak Jr, V Puybonnieux-Texier, P Quenel, et al. Public-health impact of outdoor and traffic-related air pollution: a european assessment. *Lancet*, 356(9232):795–801, 2000.

[27] HR Leider, OH Krikorian, and DA Young. Thermodynamic properties of carbon up to the critical point. *Carbon*, 11(5):555–563, 1973.

[28] EW Lemmon and RT Jacobsen. Viscosity and thermal conductivity equations for nitrogen, oxygen, argon, and air. *International Journal of Thermophysics*, 25(1):21–69, 2004.

[29] David R Lide and Thomas J Bruno. *CRC handbook of chemistry and physics*. CRC PressI Llc, 2012.

[30] F Liu, KJ Daun, V Beyer, GJ Smallwood, and DA Greenhalgh. Some theoretical considerations in modeling laser-induced incandescence at low-pressures. *Applied physics B*, 87(1):179–191, 2007.

[31] Fengshan Liu, KJ Daun, David R Snelling, and Gregory J Smallwood. Heat conduction from a spherical nano-particle: status of modeling heat conduction in laser-induced incandescence. *Applied Physics B*, 83(3):355–382, 2006.

[32] Fengshan Liu and Gregory Smallwood. Study of heat conduction between fractal aggregates and the surrounding gas in the transition regime using the dsmc method. 2008.

[33] Fengshan Liu, Min Yang, Frances A Hill, David R Snelling, and Gregory J Smallwood. Influence of polydisperse distributions of both primary particle and aggregate size on soot temperature in low-fluence lii. *Applied Physics B*, 83(3):383–395, 2006.

[34] SK Loyalka. Condensation on a spherical droplet, ii. *Journal of Colloid and Interface Science*, 87(1):216–224, 1982.

[35] SK Loyalka. Mechanics of aerosols in nuclear reactor safety: a review. *Progress in Nuclear Energy*, 12(1):1–56, 1983.

[36] Lynn A Melton. Soot diagnostics based on laser heating. *Applied optics*, 23(13):2201–2208, 1984.

[37] Farzan Memarian and KJ Daun. Prompt transient heat transfer effects in low-fluence laser induced incandescence. In *ASME International Mechanical Engineering Congress and Exposition Huston TX*, 2012.

[38] B Mewes and JM Seitzman. Soot volume fraction and particle size measurements with laser-induced incandescence. *Applied optics*, 36(3):709–717, 1997.

[39] HA Michelsen, MA Linne, Boris F Kock, Max Hofmann, B Tribalet, and C Schulz. Modeling laser-induced incandescence of soot: enthalpy changes during sublimation, conduction, and oxidation. *Applied Physics B*, 93(2-3):645–656, 2008.

[40] HA Michelsen, Fengshan Liu, Boris F Kock, H Bladh, Andreï Boïarciuc, M Charwath, T Dreier, R Hadef, Max Hofmann, J Reimann, et al. Modeling laser-induced incandescence of soot: a summary and comparison of lii models. *Applied physics B*, 87(3):503–521, 2007.

[41] Hope A Michelsen. Understanding and predicting the temporal response of laser-induced incandescence from carbonaceous particles. *The Journal of chemical physics*, 118:7012, 2003.

[42] Hope A Michelsen, Peter O Witze, David Kayes, and Simone Hochgreb. Time-resolved laser-induced incandescence of soot: the influence of experimental factors and microphysical mechanisms. *Applied optics*, 42(27):5577–5590, 2003.

[43] Dimitrios H Papadopoulos and Daniel E Rosner. Enclosure gas flows driven by non-isothermal walls. *Physics of Fluids*, 7:2535, 1995.

[44] N Pazooki, SK Loyalka, Paulo A O. Soviero, and Hugo B Resende. Heat transfer from a spherical particle in a rarefied monatomic gas. *Journal of thermophysics and heat transfer*, 2(4):324–328, 1988.

[45] Daniel U Pedersen, John L Durant, Bruce W Penman, Charles L Crespi, Harold F Hemond, Arthur L Lafleur, and Glen R Cass. Human-cell mutagens in respirable airborne particles in the northeastern united states. 1. mutagenicity of fractionated samples. *Environmental science & technology*, 38(3):682–689, 2004.

[46] H Richter and JB Howard. Formation of polycyclic aromatic hydrocarbons and their growth to soota review of chemical reaction pathways. *Progress in Energy and Combustion Science*, 26(4):565–608, 2000.

[47] Henning Richter, Silvia Granata, William H Green, and Jack B Howard. Detailed modeling of pah and soot formation in a laminar premixed benzene/oxygen/argon low-pressure flame. *Proceedings of the Combustion Institute*, 30(1):1397–1405, 2005.

[48] P Roth and AV Filippov. In situ ultra fine particle sizing by a combination of pulsed laser heat up and particle thermal emission. *Journal of aerosol science*, 27(1):95–104, 1996.

[49] Stephan Schraml, Stefan Dankers, Katharina Bader, Stefan Will, and Alfred Leipertz. Soot temperature measurements and implications for time-resolved laser-induced incandescence (tire-lii). *Combustion and Flame*, 120(4):439–450, 2000.

[50] Stephan Schraml and Stefan Will. Simultaneous measurement of soot mass concentration and primary particle size in the exhaust of a diesel engine by time-resolved laser-induced incandescence(tire-lii). 1999.

[51] Christof Schulz, Boris F Kock, Max Hofmann, Hope Michelsen, Stefan Will, Bas Bougie, Rainer Suntz, and Greg Smallwood. Laser-induced incandescence: recent trends and current questions. *Applied Physics B*, 83(3):333–354, 2006.

[52] Christopher Shaddix and Timothy Williams. Soot: Giver and taker of light the complex structure of soot greatly influences the optical effects seen in fires. *American scientist*, 95(3):238, 2007.

[53] Frederick S Sherman. A survey of experimental results and methods for the transition regime of rarefied gas dynamics. In *Rarefied Gas Dynamics, Volume 2*, volume 1, page 228, 1963.

[54] Gregory Smallwood, David Snelling, Fengshan Liu, and Omar L Gulder. Clouds over soot evaporation: errors in modeling laser-induced incandescence of soot. *Journal of heat transfer*, 123(4):814–818, 2001.

[55] David R Snelling, Fengshan Liu, Gregory J Smallwood, and Ömer L Gülder. Determination of the soot absorption function and thermal accommodation coefficient using low-fluence lii in a laminar coflow ethylene diffusion flame. *Combustion and flame*, 136(1):180–190, 2004.

[56] David R Snelling, Gregory J Smallwood, Fengshan Liu, Ömer L Gülder, and William D Bachalo. A calibration-independent laser-induced incandescence technique for soot measurement by detecting absolute light intensity. *Applied optics*, 44(31):6773–6785, 2005.

[57] DR Snelling, KA Thomson, F Liu, and GJ Smallwood. Comparison of lii derived soot temperature measurements with lii model predictions for soot in a laminar diffusion flame. *Applied Physics B*, 96(4):657–669, 2009.

[58] Dang Sheng Su, Annalucia Serafino, Jens-Oliver Müller, Rolf E Jentoft, Robert Schlögl, and Silvana Fiorito. Cytotoxicity and inflammatory potential of soot particles of low-emission diesel engines. *Environmental science & technology*, 42(5):1761–1765, 2008.

[59] Kevin A Thomson, David R Snelling, Gregory J Smallwood, and Fengshan Liu. Laser induced incandescence measurements of soot volume fraction and effective particle size in a laminar co-annular non-premixed methane/air flame at pressures between 0.5–4.0 mpa. *Applied Physics B*, 83(3):469–475, 2006.

[60] Randall L Vander Wal, Kirk A Jensen, et al. Laser-induced incandescence: excitation intensity. *Applied optics*, 37(9):1607–1616, 1998.

[61] Randy L Vander Wal and Mun Y Choi. Pulsed laser heating of soot: morphological changes. *Carbon*, 37(2):231–239, 1999.

[62] Randy L Vander Wal, Thomas M Ticich, and A Brock Stephens. Can soot primary particle size be determined using laser-induced incandescence? *Combustion and flame*, 116(1):291–296, 1999.

[63] Eckhard Vogel, Benjamin Jäger, Robert Hellmann, and Eckard Bich. Ab initio pair potential energy curve for the argon atom pair and thermophysical properties for the dilute argon gas. ii. thermophysical properties for low-density argon. *Molecular Physics*, 108(24):3335–3352, 2010.

[64] Stefan Will, Stephan Schraml, Katharina Bader, and Alfred Leipertz. Performance characteristics of soot primary particle size measurements by time-resolved laser-induced incandescence. *Applied optics*, 37(24):5647–5658, 1998.

[65] G Milton Wing and John D Zahrt. *A primer on integral equations of the first kind: the problem of deconvolution and unfolding*. Number 27. Siam, 1991.

[66] M Yang, Fengshan Liu, and Gregory J Smallwood. Application of the direct simulation monte carlo method to nanoscale heat transfer between a soot particle and the surrounding gas. 2004.

[67] Gregory D Yoder, Prasoon K Diwakar, and David W Hahn. Assessment of soot particle vaporization effects during laser-induced incandescence with time-resolved light scattering. *Applied optics*, 44(20):4211–4219, 2005.